NAFTA-GAZ

Nafta-Gaz 2026, no. 1, pp. 17–35, DOI: 10.18668/NG.2026.01.02

Resource characterization utilizing post-stack inversion to delineate gas reservoir in sand-shale sequences of Lower Indus Basin, Pakistan

Charakterystyka zasobów z wykorzystaniem inwersji po składaniu (*post-stack*) celem rozpoznania złoża gazu w sekwencjach piaskowo-łupkowych basenu dolnego Indusu w Pakistanie

Furqan M. Butt[1], Umair B. Nisar[1], Muyyassar Hussain[2], Sarfraz Khan[3], Shuja Ullah[3,4]

[1] *COMSATS University Islamabad, Pakistan*
[2] *Landmark Resources (LMKR), Pakistan*
[3] *National Centre of Excellence in Geology (NCEG), University of Peshawar, Pakistan*
[4] *Ministry of Energy, Petroleum Division, Geological Survey of Pakistan, Islamabad*

ABSTRACT: Post-stack seismic inversion is a technique that combines different types of data, particularly seismic data and well logs, and transforms a seismic volume into acoustic impedance by incorporating stratigraphic information. In this research, post-stack inversion methods were used to characterize the B-Sand interval of the Lower Goru Formation in the NIM Block, Lower Indus Basin, Pakistan, which is a gas-bearing layer, in terms of porosity and acoustic impedance. Three different inversion approaches, namely band-limited impedance inversion, sparse spike inversion, and model-based inversion, were utilized in this study using 3D seismic data and well logs to estimate reservoir properties. A comparative analysis shows that the sparse spike inversion method provides lower spatial resolution compared to the band-limited and model-based techniques. However, the inversion results from all algorithms show strong agreement with independent petrophysical analysis and log data, thereby validating the methodology. Moreover, the technique is not limited to simple gas reservoirs but also aids in the identification of tight gas sands with complex shapes, varying distribution, and complex geometries.

Keywords: post-stack inversion, acoustic impedance, sparse-spike inversion, model-based inversion, band-limited impedance inversion, porosity.

STRESZCZENIE: Inwersja sejsmiczna po składaniu (*post-stack*) to technika łącząca różne rodzaje danych, w szczególności dane sejsmiczne i dane z odwiertów, umożliwiająca przekształcenie wolumenu sejsmicznego do postaci impedancji akustycznej z uwzględnieniem informacji stratygraficznych. W niniejszej pracy metody inwersji po składaniu zastosowano do scharakteryzowania poziomu piaszczystego B kredowej formacji Lower Goru w bloku NIM w basenie dolnego Indusu w Pakistanie. Analizowany interwał stanowi poziom gazonośny i został scharakteryzowany pod kątem porowatości i impedancji akustycznej. W badaniach wykorzystano trzy różne podejścia inwersyjne: inwersję impedancji o ograniczonej szerokości pasma, inwersję rzadkich impulsów oraz inwersję opartą na modelu, wykorzystując dane sejsmiczne 3D i dane z odwiertów w celu oszacowania właściwości złoża. Analiza porównawcza wykazała, że metoda inwersji rzadkich impulsów charakteryzuje się niższą rozdzielczością przestrzenną w porównaniu z technikami o ograniczonej szerokości pasma czy opartymi na modelu. Jednocześnie wyniki uzyskane przy użyciu wszystkich algorytmów są w wysokim stopniu zgodne z niezależną analizą petrofizyczną oraz danymi z pomiarów wiertniczych, co potwierdza słuszność zastosowanej metodologii. Ponadto technika ta nie ogranicza się do prostych złóż gazu, lecz umożliwia również identyfikację piasków gazowych o złożonych kształtach i geometrii oraz zróżnicowanym rozkładzie.

Słowa kluczowe: inwersja po składaniu (*post-stack*), impedancja akustyczna, inwersja rzadkich impulsów, inwersja oparta na modelu, inwersja impedancji o ograniczonej szerokości pasma, porowatość.

Corresponding author: S. Ullah, e-mail: *shuja_nceg@uop.edu.pk*

Article contributed to the Editor: 16.06.2025. Approved for publication: 18.12.2025.

Introduction

The integrated analysis of geological methods, procedural workflows, and potential hazards constitutes a crucial approach for evaluating hydrocarbon accumulations within reservoir basins, with a central focus on characterizing key reservoir rock attributes (Torres-Verdín and Sen, 2004; Karbalaali et al., 2013). Such assessments routinely incorporate well log and seismic data (Ali et al., 2018). Acoustic impedance contrasts between subsurface lithologies generate seismic reflections that appear as amplitudes on seismic sections. Consequently, these amplitudes reflect the spatial distribution of geological contrasts (Yilmaz, 2001; Torres-Verdín and Sen, 2004; Karbalaali et al., 2013).

Seismic inversion transforms seismic reflection data into acoustic impedance models by converting interface reflectivity measurements into quantitative estimates of rock properties, defined as the product of density and P-wave velocity (Krebs et al., 2009). Acoustic impedance is a fundamental parameter in geophysical operations, as it translates seismic data into information about subsurface rock characteristics (Ali et al., 2018). The primary objective of reservoir characterization is to generate acoustic impedance models that predict essential petrophysical characteristics, including porosity, VP/VS ratio, and Poisson's ratio, which depend on lithology and fluid content (Wang, 2016). This method converts interpreted time-based reflection data into depth-based rock property models, which are more readily interpretable by geologists (Russell, 1992). The resulting impedance volumes enable quantitative interpretation through mathematical modeling to estimate reservoir properties such as porosity, fluid saturation, and lithological fractions (Hampson et al., 2001; Ali et al., 2018). Post-stack inversion analysis also facilitates the identification of reflective surfaces associated with specific sedimentary environments (Huuse and Feary, 2005). Recent studies have demonstrated its effectiveness in diverse geological settings, including gas hydrate evaluation and deep-water systems (Kumar et al., 2016; Chatterjee et al., 2016). Seismic inversion has thus become a core technology in modern hydrocarbon exploration (Ali et al., 2018).

Seismic inversion methodologies are broadly classified into pre-stack and post-stack techniques (Maurya et al., 2020). Pre-stack inversion utilizes AVO (amplitude versus offset) data from seismic records to estimate fluid and rock properties (Leite and Vidal, 2011). Post-stack inversion, typically performed at zero offset, integrates well logs, seismic, and geological data to convert seismic amplitude information into a three-dimensional volume of acoustic impedance contrasts (Downton, 2005). Specifically, post-stack inversion transforms the composite seismic wave response into acoustic impedance, a property inherent to the imaged rock types, thereby enhancing the interpretation of key geological and petrophysical boundaries within subsurface formations (Gambús-Ordaz and Torres-Verdín, 2008). This method reduces wavelet effects while improving vertical resolution of subsurface layers. The resulting acoustic impedance volumes enable the identification of different reservoir units and the inference of reservoir properties (Veeken and Da Silva, 2004). Although post-stack inversion does not incorporate shear-wave data and therefore does not allow direct fluid discrimination, it is computationally faster than pre-stack methods and remains a widely used reservoir characterization technique (Maurya and Singh, 2018).

Advanced geophysical interpretation methods are employed to evaluate the lithology and estimate reservoir porosity. Several studies have previously applied seismic interpretation, rock physics, petrophysical analysis, and structural analysis to characterize the reservoir unit of the Lower Goru Formation (Ahmed et al., 2014; Ali et al., 2018). In this study, an integrated analysis of 3D seismic attributes and post-stack inversion is conducted to predict reservoir features, particularly sand channels, which are considered the primary controls on hydrocarbon accumulation in the B-Sand interval. Accordingly, petrophysical analyses are performed to delineate the reservoir zones within the study area, predict the presence of hydrocarbon-bearing features, and distinguish lithological units (sand-shale intercalations) at well locations. Post-stack inversion algorithms are applied to analyze the spatial distribution of reservoir elastic parameters to identify potential gas-bearing zones at the target depth across the study area. Additionally, the inversion algorithms are compared to determine their relative reliability in characterizing hydrocarbon-bearing strata. Finally, geostatistical analysis is applied to identify low-impedance, sand-filled zones associated with effective porosity through time-slice mapping to delineate porous layers within the formation.

Geological setting

Pakistan is located at the junction of three lithospheric plates, namely the Arabian, Indian, and Eurasian plates. Until the Early Mesozoic (before approximately 200 Ma), the Indian Plate was part of Gondwanaland. The Sindh Monocline, which lies within the Lower Indus Basin, developed from the Jurassic to the early Cretaceous, coinciding with the northward movement of the Indian Plate (Ahmed et al., 2014). During the Late Triassic to Early Jurassic, Gondwanaland underwent counterclockwise rotation. In the Middle Jurassic, the Indian Plate separated from Gondwanaland and began moving at a rate of 3–5 cm/year. From the Late Cretaceous to the Paleocene, the western margin of the Indian Plate crossed the equator. During the Late Cretaceous, the plate attained its maximum

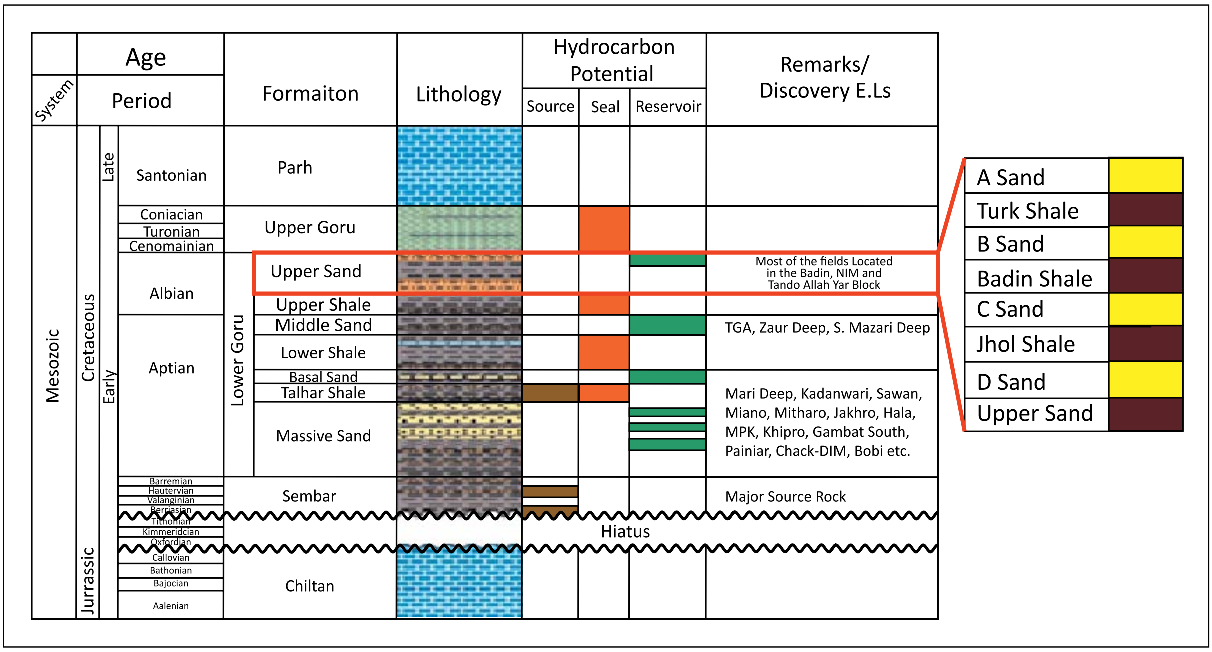

Figure 1. Generalized stratigraphy of the study area in the Lower Indus Basin. The Lower Goru Formation, of Aptian to Albian age and the focus of this study, is highlighted by the red rectangle (Baig et al., 2016)

Rysunek 1. Ogólna stratygrafia obszaru badań w basenie dolnego Indusu. Formacja Lower Goru, pochodząca z okresu od aptu do albianu i będąca przedmiotem niniejszych badań, została zaznaczona czerwonym prostokątem (Baig i in., 2016)

velocity of about 15–20 cm/year and passed over a mantle thermal center located at 70° S latitude and 72° E longitude, accompanied by counterclockwise rotation. The collision of the Indian Plate with the southern margin of the Eurasian Plate occurred during the Late Paleocene to Eocene, at which time the spreading rate decreased to approximately 4–6 cm/year. The final collision with the Eurasian Plate took place during the Eocene-Oligocene, resulting in the formation of the Himalayan Mountains. The onset of this continent-continent collision is referred to as the Maastrichtian event (Abbasi et al., 2015; Ahmed, 2018; Ahmed et al., 2018).

The Lower Indus Basin, located on the Indian Plate, experienced significant extensional phases from the Permian to the Middle Jurassic, culminating in its separation from Somalia during the Late Jurassic to Early Cretaceous (Ahmad et al., 2004). The petroleum system of this basin, which has shown a high exploration success rate over the past three decades, consists of the Sember Formation as the primary source rock and the overlying Lower Goru Formation as the main reservoir (Jamil et al., 2012). Consequently, numerous studies have focused on the petroleum system of the Lower Indus Basin (Droz and Bellaiche, 1991). Recent studies identify the Lower Goru Formation as a principal reservoir unit with widespread distribution across the Middle and Lower Indus Basin (Sheikh and Giao, 2017). Despite its extensive areal coverage, the Lower Goru Formation exhibits heterogeneity in reservoir properties and thickness (Ali et al., 2018). These variations are mainly attributed to complex shale intercalations, variable shale distribution patterns, and depositional conditions during the Cretaceous Period, leading to repeated efforts to define and quantify reservoir characteristics (Anwer et al., 2017; Ali et al., 2018).

In the study area, the Sember and Lower Goru Formations represent the most significant packages. Seven members are identified within these formations, namely the Upper Sand, Upper Shale, Middle Sand, Lower Shale, Basal Sand, Talhar Shale, and Massive Sand (Abbasi et al., 2015) (Figure 1). The Upper Shale, Lower Shale, Talhar Shale, and Sember Formation constitute the primary source rocks in this study area. The Upper Sand unit is further subdivided into A, B, C, and D sands, which are interbedded with shale and mudstone (Wandrey et al., 2004). These A, B, C, and D sand units represent the major hydrocarbon-producing reservoirs in the area and exhibit high porosity values, indicating that oil migrated from the Sember Formation through carrier beds while preserving the original porosity present at the time of migration (Ahmed et al., 2014). The Chiltan Limestone, which underlies the Sember Formation, has a conformable contact with it (Khalid et al., 2018). The project area, referred to as the "NIM Block" is located within the districts of Hyderabad and Tando Allahyar in Sindh Province, Pakistan (Figure 2). It covers a total area of 235.26 sq. km and is jointly operated by the Oil and Gas Development Company (OGDC) (95%) and Government Holdings Private Limited (GHPL) (5%). Geologically, the area lies within the Lower Indus Basin, south of the Southern Sindh Monocline.

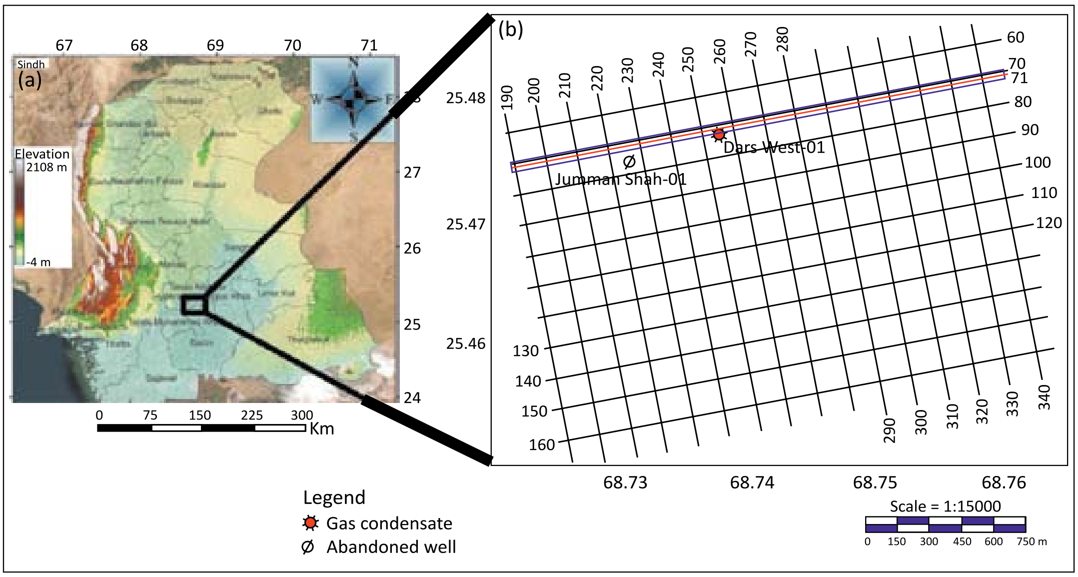

Figure 2. a) Elevation map of Sindh, Pakistan (Zehra and Afsar, 2016); b) Base map of the NIM Block, showing the location of wells and in-line No. 71 highlighted in red

Rysunek 2. a) Mapa wysokościowa prowincji Sindh w Pakistanie (Zehra i Afsar, 2016); b) Mapa bazowa bloku NIM, z zaznaczoną na czerwono lokalizacją odwiertów i linii nr 71

Methodology

A commonly used technique for predicting reservoir properties is the inversion of seismic data into acoustic impedance. Acoustic impedance inversion is applied for both descriptive and analytical evaluation of seismic data. The specific steps for the inversion techniques employed in this study are illustrated in Figure 3 and are discussed in the relevant sections. The validity of the inversion algorithms was verified by comparing petrophysical information derived from well logs with the inverted seismic data. Brief descriptions of the inversion and petrophysical methods applied in this study are provided in the following sections.

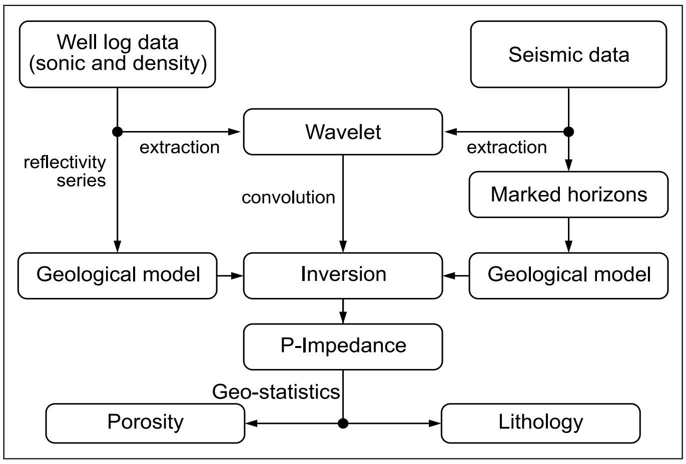

Figure 3. Generalized workflow for seismic post-stack inversion (Ali et al., 2018)

Rysunek 3. Ogólny przebieg pracy w przypadku inwersji sejsmicznej po składaniu (Ali i in., 2018)

Petrophysics

The objectives of petrophysical analysis are to determine the physical properties and behavior of reservoir rocks within the reservoir zone (Asquith et al., 2004). Well-log data are valuable for estimating porosity, shale volume, fluid saturation, and subsurface reservoir permeability. Accordingly, petrophysical assessments are applied within reservoir intervals of varying geometries to classify hydrocarbon-bearing zones. In the field of petrophysics, water and hydrocarbon saturation were computed based on estimates of shale volume, density, effective porosity, and sonic porosity.

Seismic inversion

This section provides the theoretical background of the seismic inversion methods employed in this study.

Wavelet extraction

Seismic inversion is fundamentally based on the convolutional model, which states that a synthetic seismic trace, $S(t)$, can be expressed as the convolution of the Earth's reflectivity with a selected wavelet (Barclay et al., 2008; Cooke and Cant, 2010). Mathematically, this relationship is given by:

$$S(t) = W(t) \cdot R + N \tag{1}$$

where:

$W(t)$ – extracted statistical wavelet,
R – reflection coefficient series,
N – random noise.

In this study, a constant-phase wavelet (Figure 4) was computed to ensure correlation between the inverted reflectivity

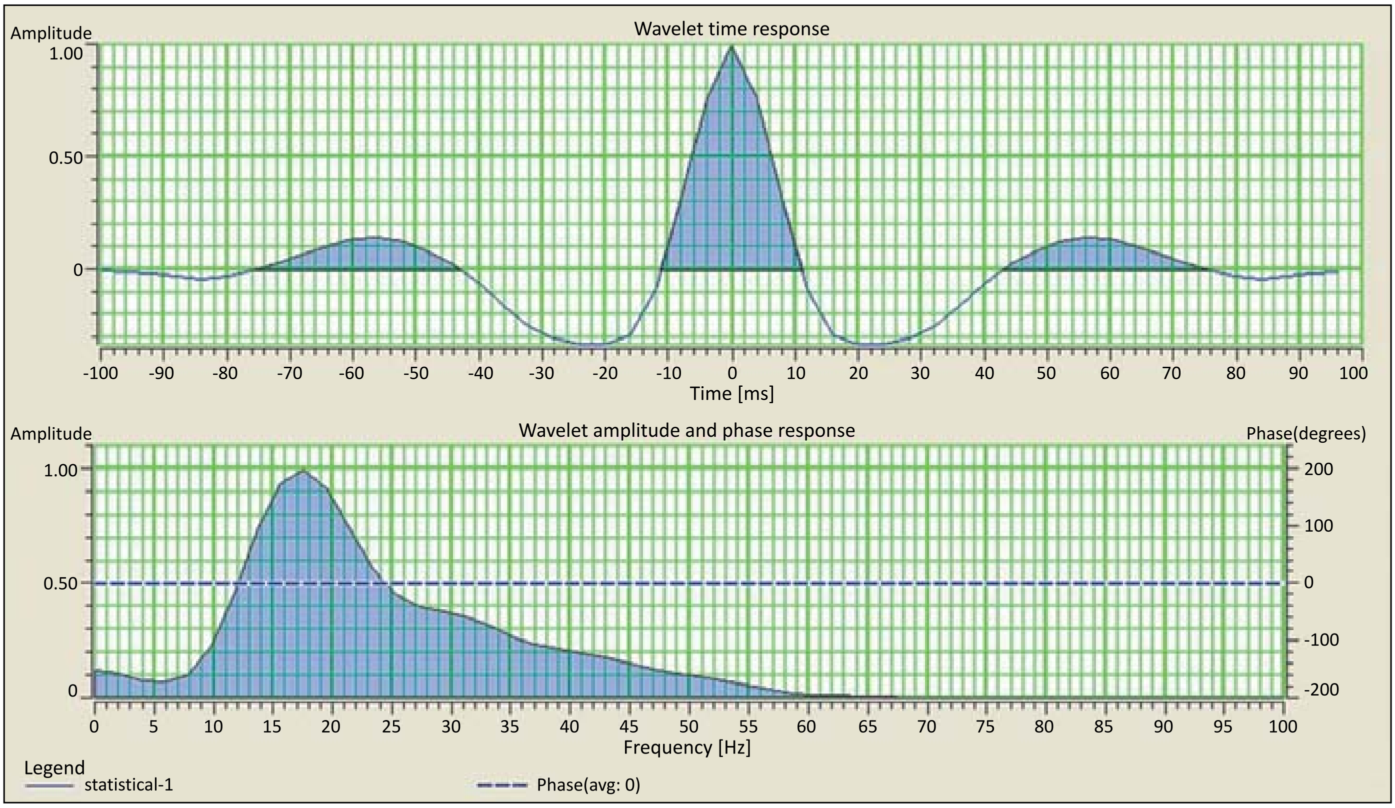

Figure 4. Statistical wavelet extracted from seismic data, showing amplitude and phase spectra. The dotted line represents the average phase of the wavelet

Rysunek 4. Fala statystyczna wyodrębniona z danych sejsmicznych, przedstawiająca widma amplitudy i fazy. Linia przerywana przedstawia średnią fazę fali

derived from seismic data and the reflectivity extracted at Jumman Shah-01 well.

The wavelet extraction was performed over a time window ranging from 900 ms to 2000 ms, with a characteristic wavelength of 100 ms. To ensure robustness, the extraction procedure incorporated both seismic data and all available well-log information. Ideally, the extracted wavelet should exhibit zero or minimum phase characteristics to ensure reliable seismic interpretation and inversion results. The phase characteristics of the input wavelet significantly influence inversion accuracy; greater phase shifts generally result in increased errors in the estimated impedance (Jain, 2013). Consequently, accurate estimation and validation of wavelet phase are essential for minimizing uncertainty and enhancing the reliability of inversion results.

Low-frequency model

Two types of acoustic impedance are commonly distinguished: (a) relative acoustic impedance and (b) absolute acoustic impedance. Relative acoustic impedance is obtained without incorporating a low-frequency model and is therefore considered a relative layer attribute. It is primarily used for a qualitative seismic analysis to identify stratigraphic features and relative variations between lithologic units. In contrast, absolute acoustic impedance represents a layer property applicable to both qualitative and quantitative analyses, enabling more comprehensive reservoir characterization (Cooke and Cant, 2010).

Absolute acoustic impedance can be derived by incorporating an appropriate low-frequency component, typically in the range of 0–15 Hz, into the inversion process (Cooke and Cant, 2010). In sparse-spike inversion, the low-frequency model is supplied separately, whereas in model-based inversion, low-frequency information is directly integrated into the inversion procedure (Cooke and Schneider, 1983). The low-frequency model constructed for model-based inversion is illustrated in Figure 5. This model must be derived from well-log data to ensure geologically consistent and realistic results, as it provides the necessary constraint for absolute impedance estimation (Lindseth, 1979).

Several approaches have been proposed to improve the accuracy of low-frequency model construction, including generalized linear inversion methods and autoregressive processes (Cooke and Schneider, 1983; Oldenburg et al., 1983) combined with linear application algorithms. Despite these methodological advancements, the problem of non-uniqueness persists, as multiple models can produce seismic responses that fit the observed data equally well (Gavotti et al., 2013).

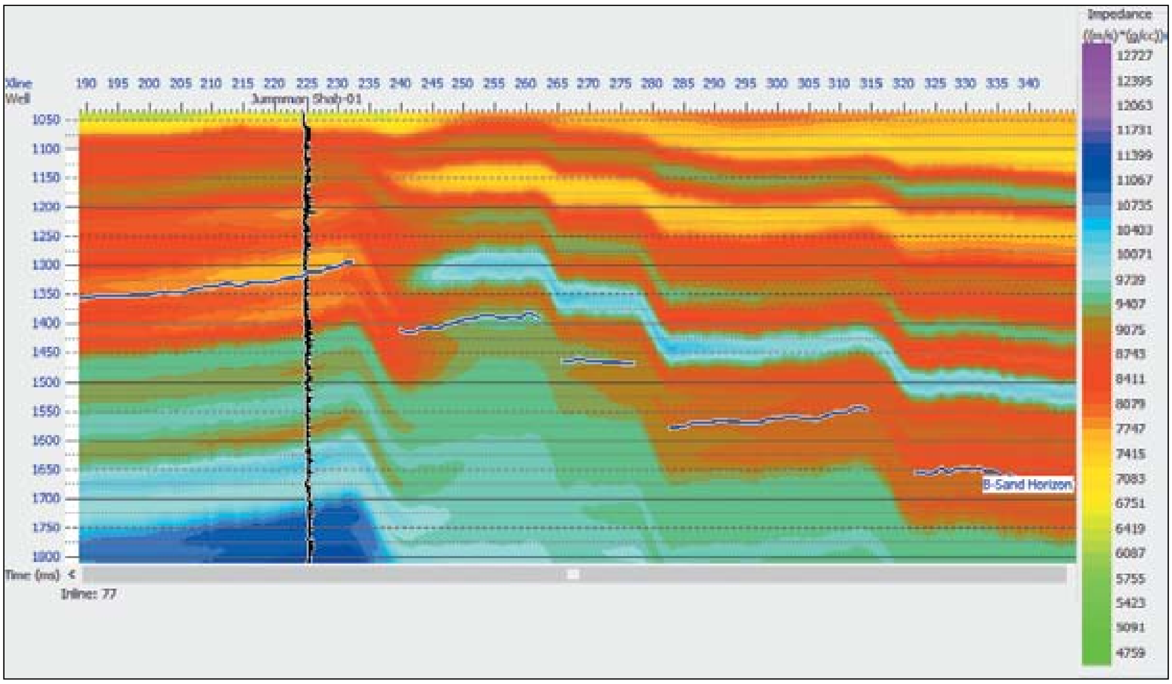

Figure 5. Low-frequency impedance model generated for application in model-based, sparse-spike, and band-limited impedance inversion

Rysunek 5. Model niskiej częstotliwości wygenerowany do zastosowania w inwersji opartej na modelu, inwersji o ograniczonej szerokości pasma i inwersji o rzadkich impulsach

Low-impedance model

A low-impedance model is generated using constrained sparse-spike inversion algorithms applied to the input seismic data. By convolving the seismic wavelet with the inverted reflectivity series within a defined acoustic impedance range, a model capturing the fundamental subsurface features is produced. Interpolation and extrapolation techniques, including trigonometric interpolation, inverse distance weighting, and kriging, are employed to integrate all available data, such as impedance logs and interpreted stratigraphic horizons, thereby enhancing model reliability (Ali et al., 2018). The low-frequency component is subsequently added to the inverted seismic volume to improve resolution and ensure consistency of the inversion results. The resulting acoustic impedance cube is calibrated against measured rock properties to establish a robust relationship between seismic characteristics and petrophysical data (Ibrahim, 2007). Figure 6 illustrates the low-impedance model developed in this study for sparse-spike inversion and band-limited impedance inversion, highlighting the integration of seismic and well-log data for accurate subsurface characterization.

Algorithm of model-based inversion

Model-based seismic inversion commonly employs a linear inversion algorithm, assuming that both the seismic trace, $S(t)$, and the wavelet, $W(t)$, are known. The program repeatedly modifies an initial geological model until the synthetic trace matches the observed seismic trace within an acceptable tolerance (Gavotti et al., 2013, 2014). The inversion process systematically updates the subsurface model to minimize the discrepancy between observed and synthetic seismic responses by solving the objective function presented in equation (2), which quantifies the misfit between actual and synthetic data (Gavotti et al., 2013). This can be expressed as:

$$J = \text{weight}_1\, x(S - W \cdot R) + \text{weight}_2\, x(M - H \cdot R) \qquad (2)$$

where:

S – observed seismic trace,
W – statistically extracted wavelet,
R – reflection coefficient series,
M – initial guess model,
H – integration operator convolved with the final reflectivity to generate the impedance model.

In this equation, the first term represents seismic trace reconstruction, while the second term constrains impedance estimation based on the first model. Well-log data are incorporated to mitigate the effects of random noise and minor modeling errors, thereby improving the stability and reliability of the inverted results. This approach emphasizes the importance of iterative refinement and multi-domain calibration in generating geologically consistent impedance models.

Algorithm of sparse-spike inversion

The sparse-spike inversion applied in this study is based on the linear programming approach introduced by Li (2001).

Sparse-spike inversion aims to extract the reflection coefficient series and a frequency band from seismic data to reconstruct a subsurface model that incorporates both high- and low-frequency components (Banihasan, 2006; Ali et al., 2018). When seismic data $x(t)$ and source wavelets are used as inputs, acoustic impedance is obtained as the output (Ontiveros et al., 2014). Based on the preceding, the relationship between the data vector $b = (b_1, b_2, .., b_n)$, the model vector $a = (a_1, a_2, .., a_n)$, and noise n can be expressed as:

$$Za + n = b \tag{3}$$

where: Z is the operator that quantifies the mismatch that is in between the model and the data. The model vector (a), defined by the probability $p(a|b)$, can be represented using Bayes' formula as shown in the equation below:

$$p(a\,|\,b) = \frac{p(b\,|\,a)p(a)}{p(b)} \tag{4}$$

where: $p(a)$ and $p(b)$ represent the initial information about the model and the data, respectively, and $p(b|a)$ defines the relationship between the model and the observations. A maximum a posteriori solution can be obtained for a system built on probability $p(a|b)$ (Ali and Jakobsen, 2014; Anwer et al., 2017). Equation (5) demonstrates how to express Y (objective function for minimization):

$$Y = -\log p(a\,|\,b) = -\log p(b\,|\,a) - \log p(a) \tag{5}$$

where: the term log $p(b)$ is omitted because it is constant. A solution for equation (11) can be obtained by optimizing the objective function Y that honors the imposed low-impedance model in a least-squares sense (Ontiveros et al., 2014).

Algorithm of band-limited impedance inversion

Band-limited impedance inversion is one of the earliest post-stack seismic inversion techniques. It produces acoustic impedance as output when seismic data are provided as input (Maurya et al., 2020). Furthermore, by applying specific estimation methods, such as geostatistical approaches, the resulting impedance can be transformed into various petrophysical properties. The relationship between the seismic trace and seismic impedance can be used to derive the mathematical formulation of the band-limited impedance system (Maurya and Singh, 2017). In this approach, the seismic trace is inverted into impedance using an equation similar to recursive inversion, with slight modifications, expressed as:

$$I_{j+1} = I_1 \exp\left(\gamma \sum_{k=1}^{j} S_k\right) \tag{6}$$

where:

I_{j+1} – seismic impedance,
I_1 – impedance at the surface,
S_k – scaled reflectivity
γ – scaling factor.

The primary limitation of this inversion approach is that it can be applied only to zero-phase seismic data; consequently, the results may not be as predicted (Maurya and Singh, 2015). The inversion procedure utilizes seismic and well-log data as input, and the resulting acoustic impedance is subsequently evaluated, as illustrated in the diagram. Owing to its simplicity and ease of implementation, this approach is still widely used by oil and gas companies for subsurface characterization.

Geostatistical analysis

In recent years, geostatistical analysis has played a critical role in the development and characterization of hydrocarbon reservoir workflows (Dubrule, 2003). Geostatistical methods are applied to seismic and well-log data to investigate relationships among parameters derived from petrophysical analysis (Doyen, 1988). Regression analysis is employed to establish a mathematical relationship between attributes extracted from seismic and well-log data under these assumptions (Ali et al., 2018). The derived relationships are then applied to the entire seismic volume to estimate porosity distribution. The resulting porosity values are compared with those measured in boreholes to assess the reliability of the predictions.

Results

Marking of horizons and identification of faults

Correlation and identification of the B-Sand horizon were carried out by integrating existing well formation tops (Table 1) with a synthetic seismogram (Figure 4). This process began with the calibration of digitized bulk density and sonic logs to the 3D seismic data. In particular, data from Jumman Shah-01 well were used to generate the synthetic seismogram. A wavelet was extracted from the seismic data within a target depth window of 1534 m to 1618 m, using both inline and crossline seismic traces. The extracted wavelet was subsequently convolved with the reflectivity series derived from sonic and density logs to generate the synthetic seismogram. After depth-to-time conversion using check-shot data, the synthetic seismogram and seismic traces were accurately calibrated to construct an impedance model represented as a series of reflection coefficients. An Ormsby wavelet was used for this dataset, with a sampling rate of 0.002 s, frequency bounds of 5, 10, 60, and 90 Hz, and a total wavelength of 0.4 s. Figure 6 illustrates the well-to-seismic tie, showing the synthetic seismogram, reflectivity series, and the extracted wavelet, with the B-Sand formation at the well location highlighted in red. Structural interpretation of the seismic data (Figure 7) identified four distinct normal faults (Fault-1, Fault-2, Fault-3, and Fault-4), indicating an extensional regime in the region. Well data are used as a pre-mapping tool to determine and track the spatial extent of the B-Sand interval within the Lower Goru Formation (Figure 8). To characterize and evaluate hydrocarbon zones within the B-Sand interval, model-based, sparse-spike, and band-limited impedance inversion methods were applied to the interpreted data. A further objective was to compare the performance of these inversion techniques to determine which method is most effective for identifying hydrocarbon-bearing zones within the formation.

Within a defined time window, including both inline and crossline traces, the wavelet was extracted from the seismic data, after which model-based, sparse-spike, and band-limited impedance inversions were applied to the seismic dataset of the NIM block.

Petrophysics

Petrophysical evaluation is a fundamental component of subsurface reservoir characterization, providing preliminary insights into geological settings and reservoir parameters. Wireline log interpretation plays a critical role in this process by enabling the identification of prospective hydrocarbon-bearing intervals. Gas-prone zones are commonly recognized through a combination of diagnostic log responses, including low to moderate gamma-ray values, negative deflections on spontaneous potential (SP) logs, elevated resistivity readings, reduced density and neutron porosity values, and lower acoustic velocities. These integrated responses collectively delineate reservoir quality and hydrocarbon potential.

The petrophysical properties of the B-Sand interval within the Lower Goru Formation were evaluated using wireline data from Jumman Shah-01 and Dars West-01 wells. Detailed petrophysical results are summarized in Table 1, while graphical interpretations are presented in Figures 9 and 10. Shale volume V_{sh} was estimated from gamma-ray (GR) logs, which serve as indicators of lithological composition. Higher GR values correspond to increased shale content, whereas lower GR values indicate sand-rich intervals with higher porosity and permeability.

GR logs from both wells clearly differentiate sand and shale units, with values greater than 85 API interpreted as shale and values below 85 API interpreted as sand. Average GR values of approximately 35 API in Jumman Shah-01 and 40 API in Dars West-01 indicate that the B-Sand reservoir is predominantly composed of clean sand. The calculated shale volumes V_{sh} of 18% in Jumman Shah-01 and 20% in Dars West-01 further support the interpretation of a sand-dominated reservoir with minimal shale content. These results indicate the favorable reservoir quality of the B-Sand interval, characterized by low shale concentration and enhanced porosity and permeability. Petrophysical parameters derived from wireline log analysis provide important insights into reservoir quality and hydrocarbon potential. In Jumman Shah-01 well, total porosity (PHID), effective porosity (PHIE), and sonic-derived porosity (PORS) were estimated at approximately 22%, 16%, and 22%, respectively. In Dars West-01 well, the corresponding values were approximately 18%, 11%, and 18% (Table 1). These results indicate that both wells exhibit fair to good porosity, suggesting the presence of high-quality sand within the reservoir interval (Figures 9 and 10).

Evaluation of water saturation (S_W) further clarifies reservoir characteristics. High S_W values are indicative of water-bearing zones, whereas lower values suggest hydrocarbon saturation. In Jumman Shah-01, S_W exceeds 79%, indicating that the reservoir interval is predominantly water-saturated despite

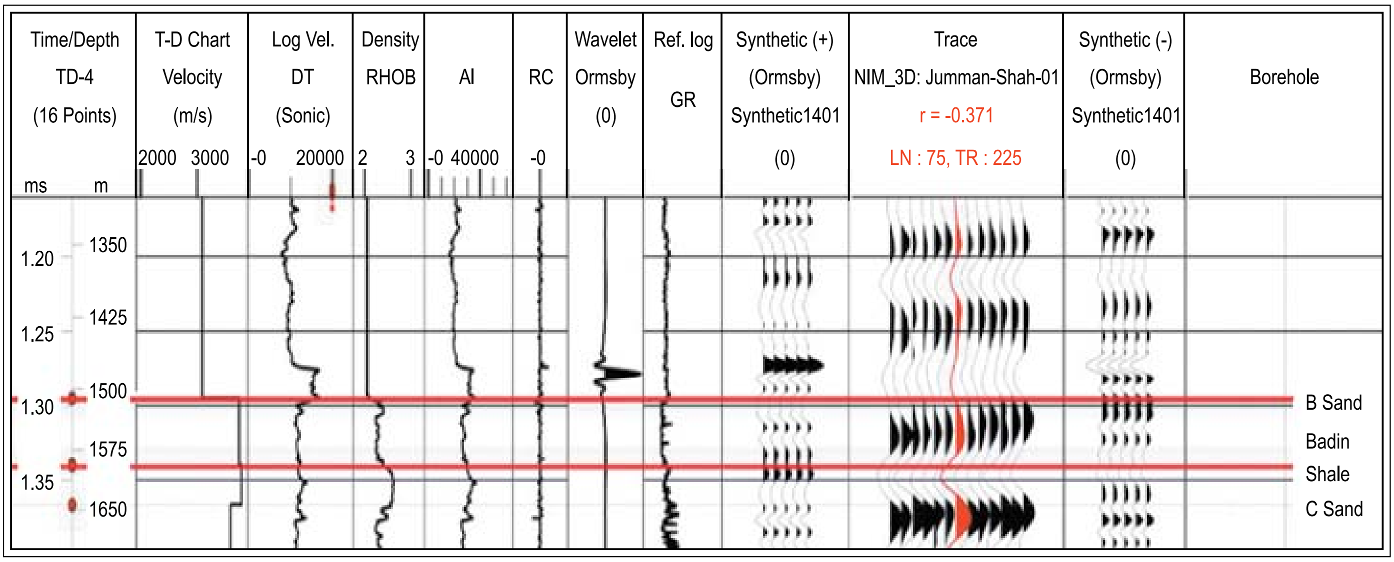

Figure 6. Data from Jumman Shah-01 well used for generating the synthetic seismogram

Rysunek 6. Dane dotyczące odwiertu Jumman Shah-01 wykorzystane do wygenerowania syntetycznego sejsmogramu

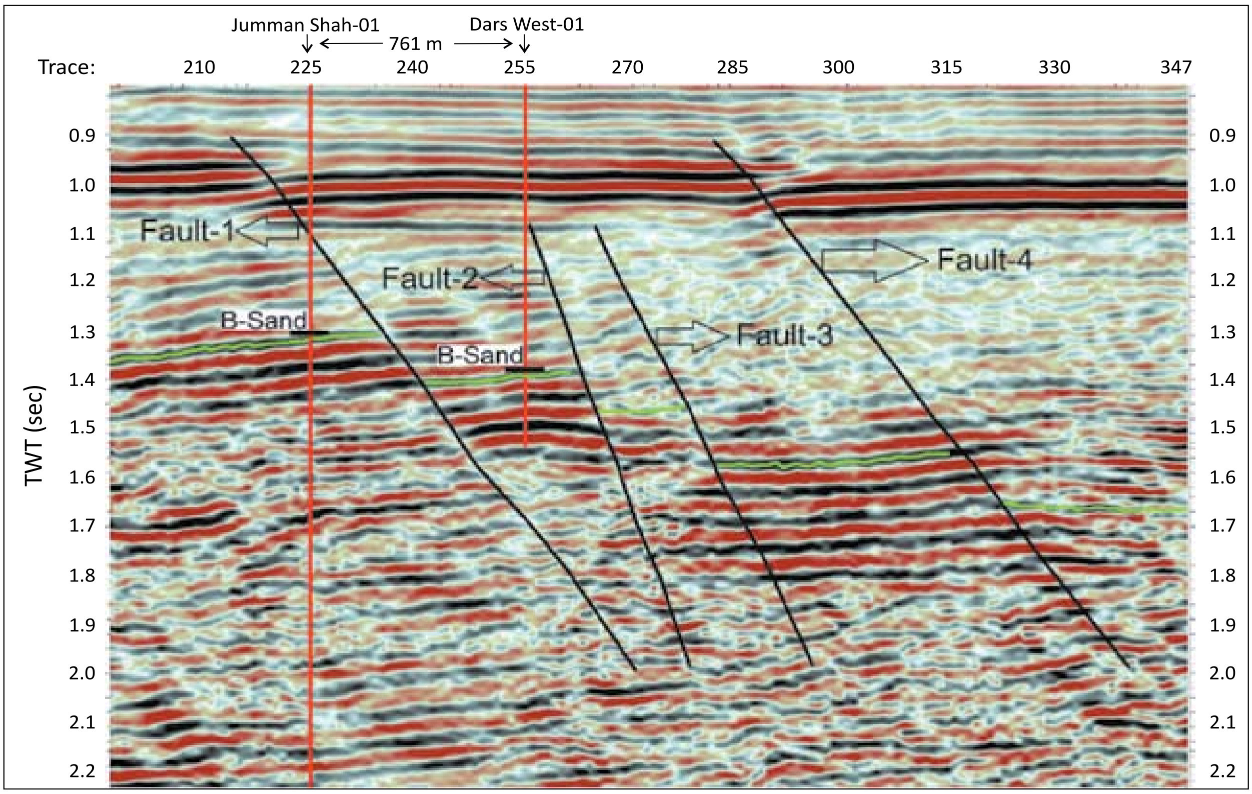

Figure 7. Seismic section (inline 71) showing marked B-Sand (green),Two Way Time (TWT) of 1.3 second, faults (black) and well (red)

Rysunek 7. Sekcja sejsmiczna (linia 71) pokazująca zaznaczony poziom piaszczysty B (kolor zielony), czas dwukierunkowy (TWT) wynoszący 1,3 sekundy, uskoki (kolor czarny) i odwiert (kolor czerwony)

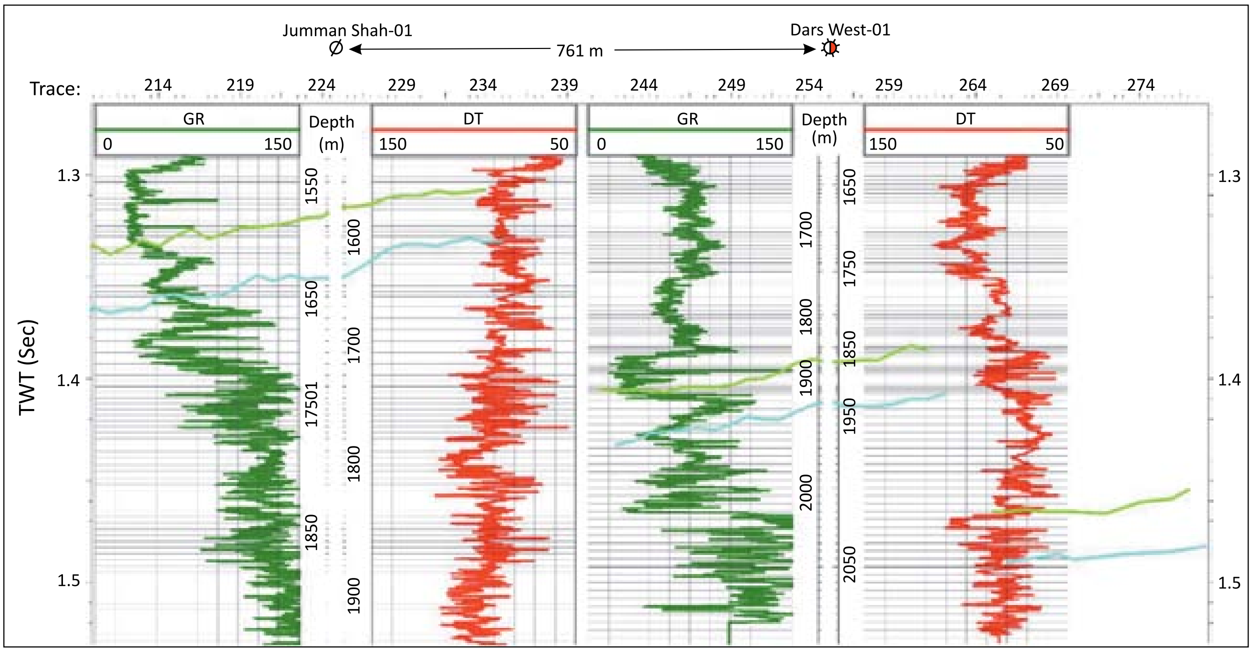

Figure 8. Well correlations based on gamma-ray and sonic (DT) logs, showing the top of B-Sand (green). The blue line represents the top of the Badin Shale. The total thickness of the B-Sand can also be analyzed from this. The correlation illustrates the spatial distribution of B-Sand within the Lower Goru Formation. The B-Sand interval in the Lower Goru Formation comprises the main reservoir interval in the study area

Rysunek 8. Korelacje dla odwiertów oparte na pomiarach promieniowania gamma i sonicznych (DT) pokazujące górną granicę poziomu piaszczystego B (kolor zielony). Niebieska linia przedstawia górną granicę warstwy łupków w rejonie Badin. Na tej podstawie można również przeanalizować całkowitą grubość poziomu piaszczystego B. Korelacja ilustruje rozmieszczenie przestrzenne poziomu piaskowego B w formacji Lower Goru. Odcinek poziomu piaszczystego B w formacji Lower Goru stanowi główny odcinek zbiornika w badanym obszarze

Table 1. Petrophysical parameters of the B-Sand encountered in the studied wells

Tabela 1. Parametry petrofizyczne poziomu piaskowego B występującego w badanych odwiertach

Sr. no.	Well name	Depth	V_{sh}	PHID	PHIE	PORS	S_w	S_{hc}
		[m]	[%]					
1	Dars West-01	1852–1944	20.5	18.6	11.0	18.42	43.7	56.30
2	Jumman Shah-01	1534–1618	18.6	22.6	16.98	22.48	79.75	20.25

favorable porosity. In contrast, S_W in Dars West-01 is greater than 43%, implying a considerably higher hydrocarbon content within the B-Sand reservoir.

Overall, these petrophysical results highlight contrasting fluid saturation conditions between the two wells, with Jumman Shah-01 being water-dominated and Dars West-01 exhibiting more favorable hydrocarbon saturation. This distinction underscores the importance of integrating porosity and saturation analyses for robust reservoir characterization and hydrocarbon prospect assessment.

Seismic inversion

Wavelets were extracted from seismic data, including inline and crossline traces, over a specific time window. The extracted

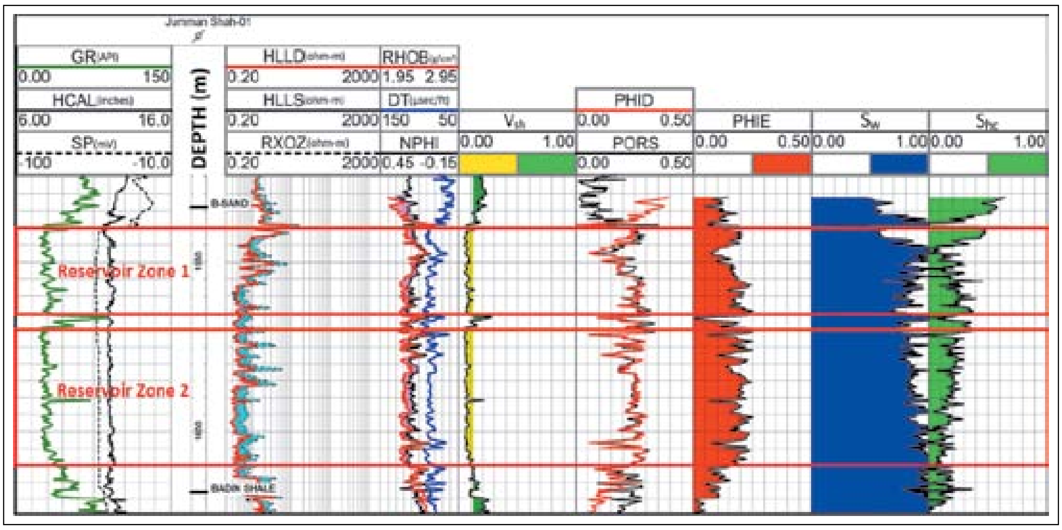

Figure 9. Petrophysical interpretation of the B-Sand in Jumman Shah-01, showing calculated V_{sh}, PHID, PHIE, PORS, S_W and S_{hc}

Rysunek 9. Interpretacja petrofizyczna poziomu piaszczystego B w Jumman Shah-01, przedstawiająca obliczone wartości V_{sh}, PHID, PHIE, PORS, S_W i S_{hc}

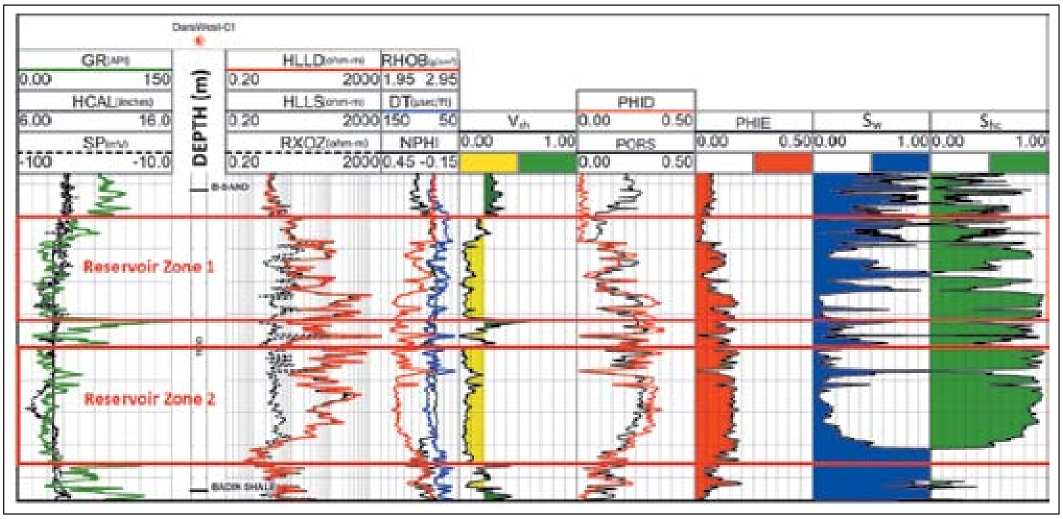

Figure 10. Petrophysical interpretation of the Dars West-01, showing calculated V_{sh}, PHID, PHIE, PORS, S_W and S_{hc}

Rysunek 10. Interpretacja petrofizyczna dla Dars West-01, przedstawiająca obliczone wartości V_{sh}, PHID, PHIE, PORS, S_W i S_{hc}

statistical wavelet was convolved with the reflectivity series derived from sonic and density logs at Jumman Shah-01 well to generate a synthetic seismogram (Figure 4). This synthetic seismogram was subsequently correlated with the observed seismic traces at the same well location, enabling direct comparison between modeled and recorded seismic responses. The correlation results, which confirm the reliability of the wavelet extraction and reflectivity estimation procedures, are presented in Figure 11. Seismic data from the NIM region are then subjected to model-based, sparse-spike, and band-limited impedance inversion. The results of these three models are presented in the following sections.

Model-based inversion

For model-based seismic inversion, a statistical zero-phase wavelet was extracted within the 1200–1700 ms time window. The wavelet is characterized by a sharp peak amplitude, high dominant frequency, and minimal side-lobe energy, ensuring improved temporal resolution and stability. The frequency and phase spectra confirm its accuracy (Figure 11). At Jumman Shah-01 well, strong agreement was observed between log-derived and seismic-derived acoustic impedance within the B-Sand interval (Figure 12). Synthetic seismic traces generated by convolving the extracted wavelet with the reflectivity series showed excellent agreement with the observed traces, supported by a correlation coefficient of 0.98 and a low RMS error of 0.078 or 695 m/s * (g/cc). These results validate the reliability of the wavelet extraction and inversion methodology and demonstrate its ability to generate geologically consistent impedance models with high accuracy and minimal error.

Model-based inversion was applied to the interpreted seismic volume at in-line no. 77, and the results are presented in Figure 12. The inversion successfully captures lateral variations in acoustic impedance by incorporating a spatially constant low-frequency model, as illustrated in Figure 12. The zone of interest, the B-Sand interval, exhibits a step-faulted structure in this region, resulting in variations in time and depth. These intervals are characterized by low impedance values. The observed impedance ranges of approximately 9739–10 735 m/s * (g/cc) (light blue to dark blue colors) indicate the presence of gas within this zone (Figure 12). The step-faulting creates structural traps at different intervals, which deepen from northwest to northeast. Within the selected time window, alternating layers of high- to medium-impedance values (purple to light blue colors) are observed, reflecting interbedded sand-shale layers at this zone which is the part of the Lower Goru Formation.

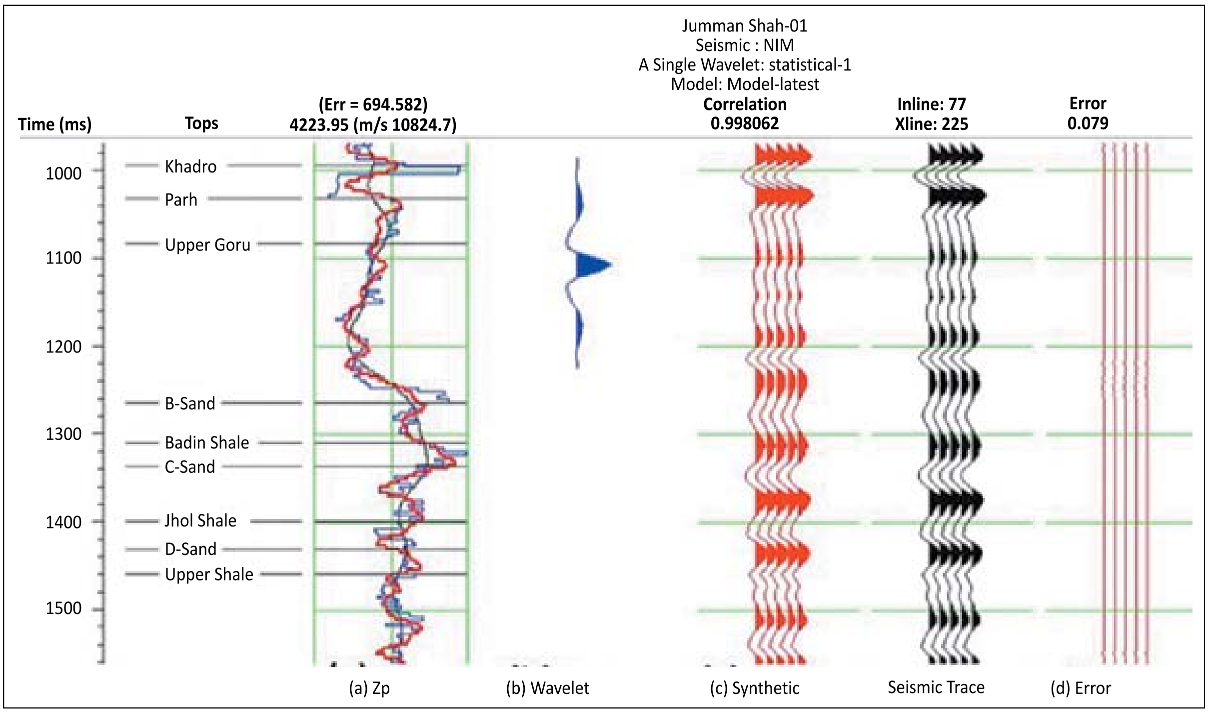

Figure 11. Model-based seismic inversion analysis at Jumman Shah-01 well compared with the initial model: (a) filtered impedance log (blue), inversion impedance log (red) and initial model (black); (b) extracted wavelet; (c) synthetic and extracted trace from inversion (red) and seismic (black) and (d) RMS error between the synthetic and seismic traces

Rysunek 11. Analiza inwersji sejsmicznej oparta na modelu w odwiercie Jumman Shah-01 w porównaniu z modelem początkowym: (a) przefiltrowany wykres impedancji (niebieski), odwrócony wykres impedancji (czerwony) i model początkowy (czarny); (b) wyodrębniona fala; (c) syntetyczny ślad z inwersji (czerwony) i ślad sejsmiczny (czarny); oraz (d) błąd RMS między śladami syntetycznymi i sejsmicznymi

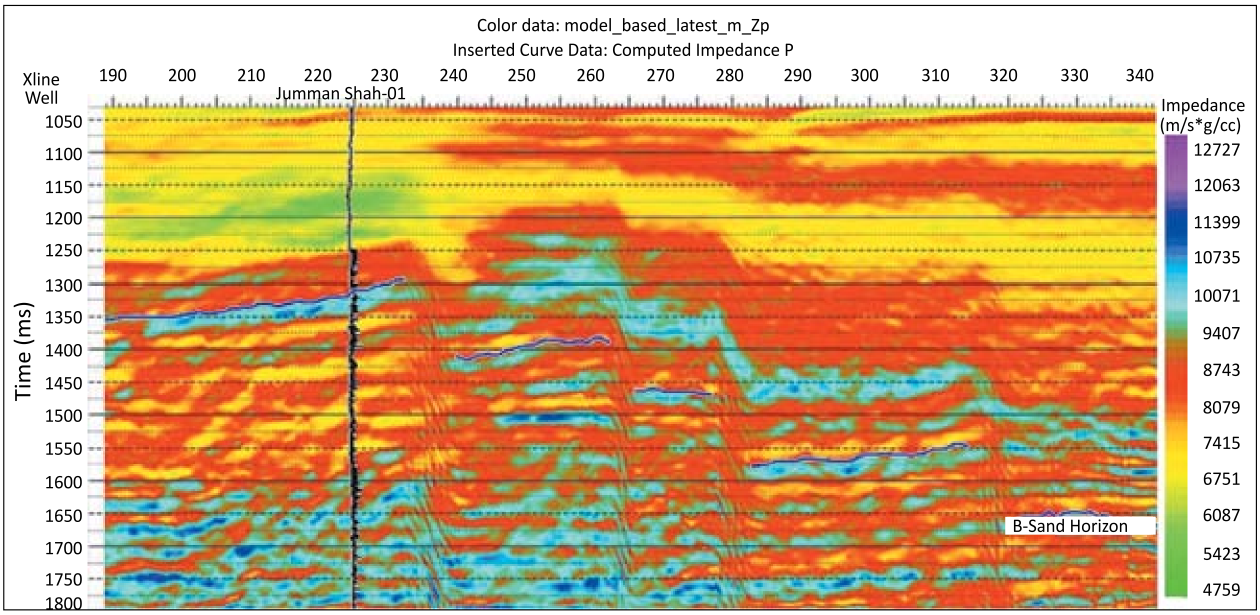

Figure 12. Model-based, sparse-spike, and band-limited impedance inversion for inline No. 77. The impedance log of Jumman Shah-01 well is also shown. Lateral lithological variations are effectively captured using this inversion algorithm

Rysunek 12. Inwersja impedancji oparta na modelu dla linii nr 77. Przedstawiono również rejestr impedancji odwiertu Jumman Shah-01. Algorytm inwersji pozwala skutecznie uchwycić boczne zmiany litologiczne

Sparse-spike inversion

For sparse-spike inversion, a statistical wavelet was extracted over the 1200–1700 ms time window, and its frequency spectrum was adjusted by correlating the observed trace with the inverted trace at Jumman Shah-01 well. As shown in Figure 13, a strong correlation coefficient of 0.99 is obtained between the

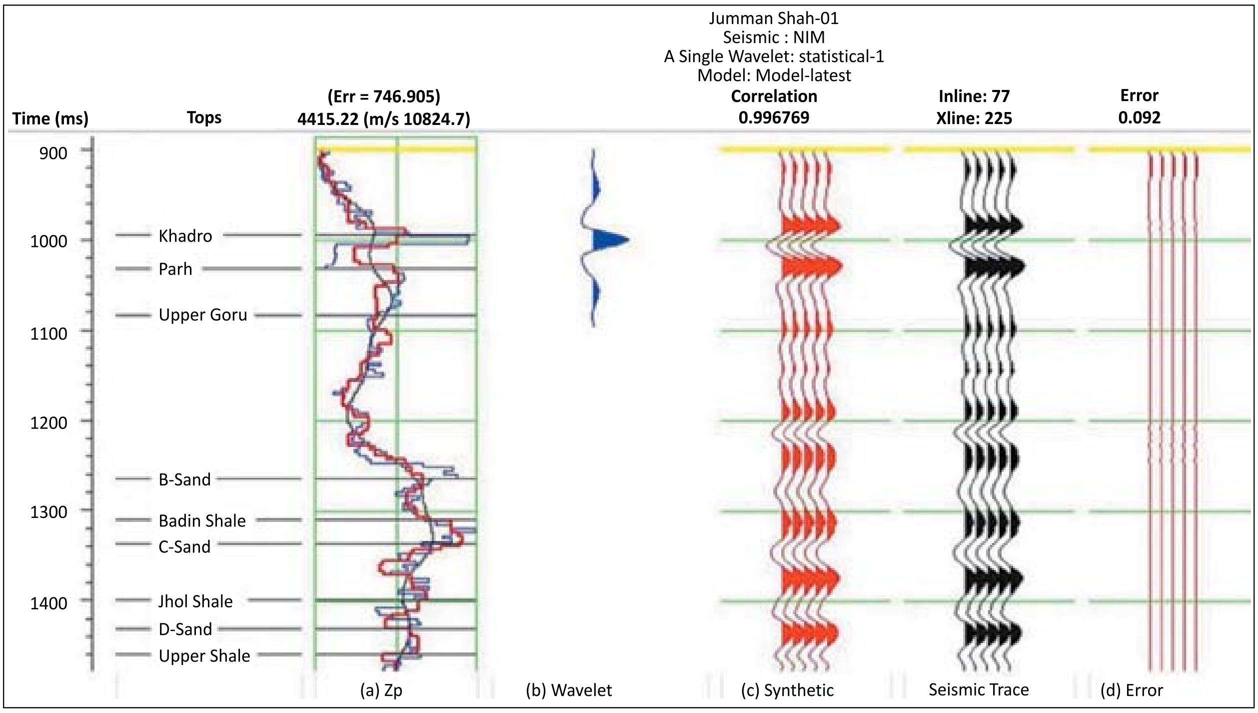

Figure 13. Sparse-spike inversion analysis at Jumman Shah-01 well compared with the initial model: (a) filtered impedance log (blue), inversion impedance log (red) and initial model (black); (b) extracted wavelet; (c) synthetic and extracted trace from inversion (red) and seismic (black); and (d) RMS error between the synthetic and seismic traces.

Rysunek 13. Analiza inwersji rzadkich impulsów w odwiercie Jumman Shah-01 w porównaniu z modelem początkowym: (a) przefiltrowany wykres impedancji (niebieski), odwrócony wykres impedancji (czerwony) i model początkowy (czarny); (b) wyodrębniona fala; (c) syntetyczny ślad z inwersji (czerwony) i ślad sejsmiczny (czarny); oraz (d) błąd RMS między śladami syntetycznymi i sejsmicznymi synthetic (red) and seismic (black) traces, with an RMS impedance error of 0.09, corresponding to 747 m/s * (g/cc). The results of sparse-spike inversion applied along inline No. 77 are presented in Figure 12. The B-Sand horizon is clearly identified and exhibits low impedance values represented by light blue colors, with an impedance range of 9700–10 100 m/s * (g/cc). Above the B-Sand interval (light blue layer), another high impedance layer corresponding to the Upper Goru Formation is observed (blue-dark blue), with impedance values ranging from 10 500 to 11 000 m/s * (g/cc). This layer acts as a seal, while the underlying low-impedance B-Sand layer indicates the presence of gas within the reservoir.

Band-limited impedance inversion

The inversion analysis was performed at the location of Jumman Shah-01 well using a time window of 1200–1700 ms. As shown in Figure 12, the correlation coefficient is 0.955, with an associated error of 729.38 m/s * (g/cc). The results of the band-limited impedance inversion are comparable to those obtained from the sparse-spike inversion. The inverted impedance cross-section for inline No. 77 is shown in Figure 14. The formation impedance varies within a range of 9739–11067 m/s * (g/cc) (light blue color), indicating relatively low impedance values. This low-impedance range suggests the presence of unconsolidated sediments and supports the interpretation that the formation is predominantly composed of sand deposits. The low impedance values further indicate gas accumulation within the sand-rich intervals.

Porosity determination

Cross-plots of acoustic impedance versus porosity are presented in Figures 15 and 16 (Jumman Shah-01 and Dars West-01 wells). The correlation coefficients are relatively high and were determined using a linear regression approach. In this study, geologically interpretable relationships were prioritized, as the relationship between estimated porosity and acoustic impedance is linear in nature. Accordingly, a linear regression method was employed. Within the resolution limits of well-log and seismic data, this linear relationship is considered valid. In this specific case, the application of higher-order polynomial fits would be inappropriate and potentially misleading, as such relationship would be difficult to interpret. Consequently, porosity estimates derived from inverted acoustic impedance are regarded as accurate and practically applicable within this unique geological setting. Average values at the well locations (Jumman Shah-01 and Dars West-01) were used to construct the cross-plots between acoustic impedance and porosity shown in Figures 15 and 16. The linear relationships established

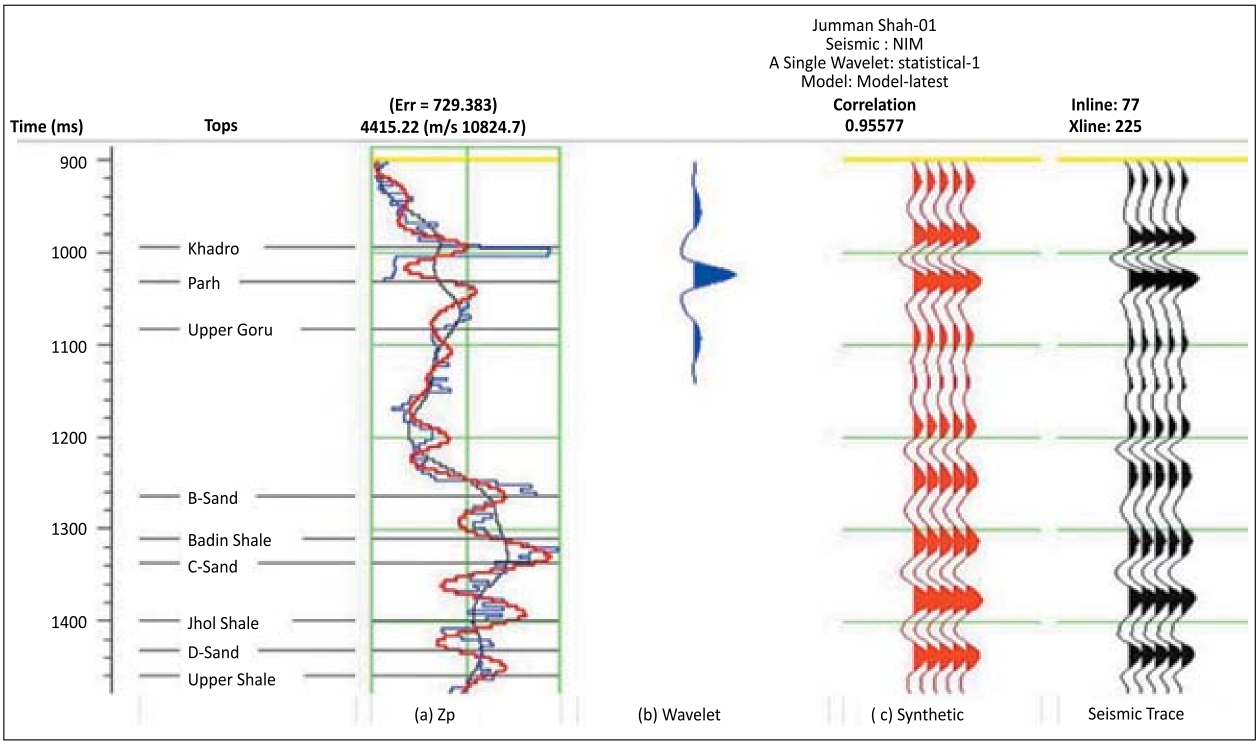

Figure 14. Band-limited impedance inversion analysis at Jumman Shah-01 well compared with the initial model: (a) filtered impedance log (blue), inversion impedance log (red), and initial model (black); (b) extracted wavelet; (c) synthetic and extracted trace from inversion (red) and seismic (black)

Rysunek 14. Analiza odwrócenia impedancji o ograniczonej szerokości pasma w odwiercie Jumman Shah-01 w porównaniu z modelem początkowym: (a) przefiltrowany wykres impedancji (niebieski), odwrócony wykres impedancji (czerwony) i model początkowy (czarny); (b) wyodrębniona falka; oraz (c) syntetyczny ślad z inwersji (czerwony) i ślad sejsmiczny (czarny) between acoustic impedance and porosity using best-fit lines are expressed as:

$$\varphi = (-3.53 \times 10^{-5}) \times A + 0.466 \tag{7}$$

$$\varphi = (-2.31 \times 10^{-5}) \times A + 0.330 \tag{8}$$

where:

φ – porosity,

A – inverted impedance volume generated from model-based inversion.

Figures 14 and 15 illustrate the acoustic impedance distribution within the B-Sand interval, showing relatively low impedance values ranging from 8065 to 10011 m/s * (g/cc) in Jumman Shah-01 and from 8209 to 9939 m/s * (g/cc) in Dars West-01. The cross-plots demonstrate strong correlations between acoustic impedance and porosity, with correlation coefficients of 0.72 for Jumman Shah-01 and 0.86 for Dars West-01, thereby confirming the reliability of the inversion-derived porosity estimates.

The inverted impedance surface of the B-Sand interval, obtained from the model-based post-stack inversion algorithm (Figure 12), was subsequently converted into porosity using equations (7) and (8). Time-slice analysis consistently indicates that low-impedance zones within the B-Sand interval exhibit a NE-NW orientation, corresponding to a favorable distribu-

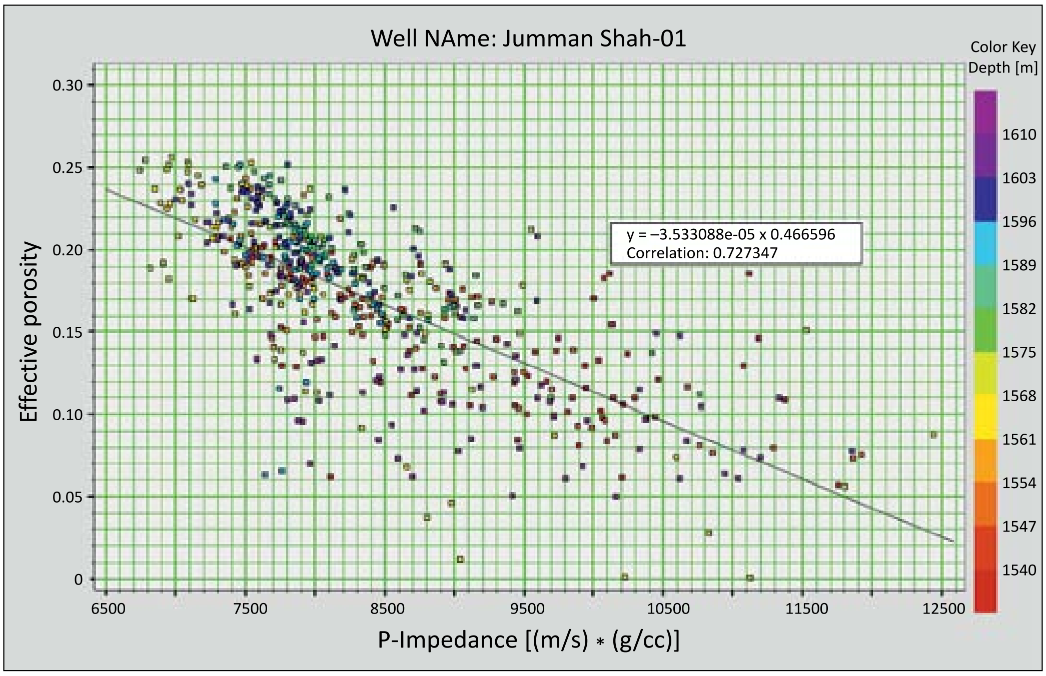

Figure 15. Cross-plot of acoustic impedance (AI) versus effective porosity for Jumman Shah-01, showing an acceptable correlation coefficient. Porosity and acoustic impedance exhibit a linear relationship with a negative slope

Rysunek 15. Wykres krzyżowy impedancji akustycznej w funkcji porowatości efektywnej dla odwiertu Jumman Shah-01, wykazujący akceptowalny współczynnik korelacji. Porowatość i impedancja akustyczna wykazują liniową zależność o ujemnym nachyleniu

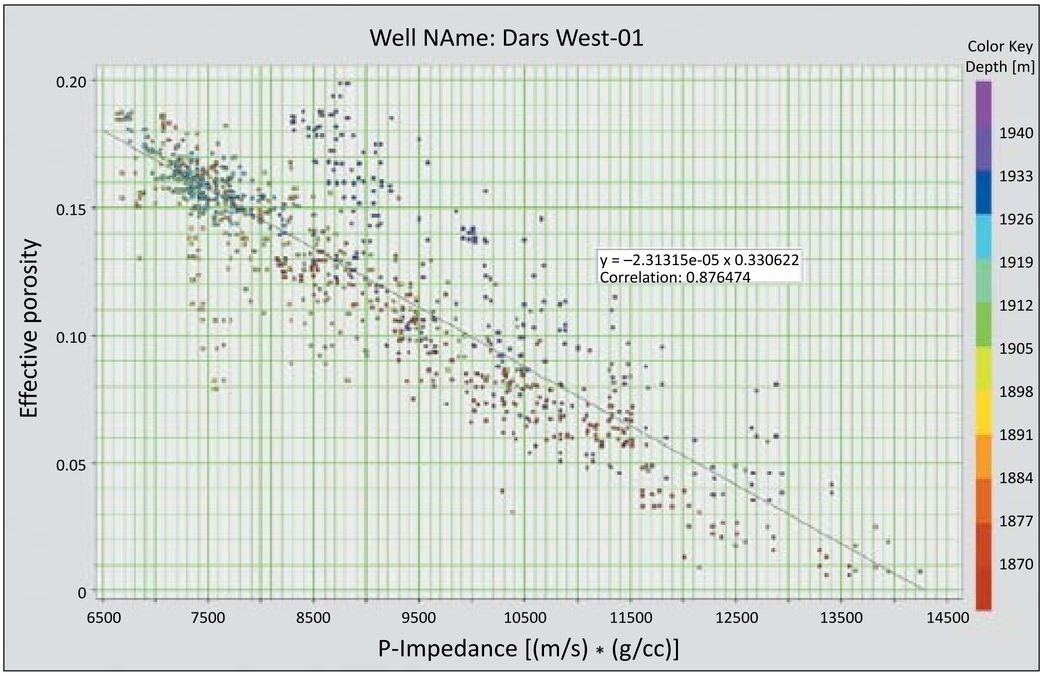

Figure 16. Cross-plot of acoustic impedance (AI) versus effective porosity for Dars West-01, showing an acceptable correlation coefficient. Porosity and acoustic impedance exhibit a linear relationship with a negative slope

Rysunek 16. Wykres krzyżowy impedancji akustycznej w funkcji porowatości efektywnej dla odwiertu Dars West-01, wykazujący akceptowalny współczynnik korelacji. Porowatość i impedancja akustyczna wykazują liniową zależność o ujemnym nachyleniu tion of porosity along this structural trend. Figures 17 and 18 further illustrate the spatial variability in reservoir quality between the two wells.

Figure 19 and 20 show that Jumman Shah-01 exhibits medium-to-high porosity values (represented by dark red to purple), whereas Dars West-01 displays low-to-medium porosity (dark red to yellow). Despite the higher porosity observed in Jumman Shah-01, petrophysical analysis indicates a higher hydrocarbon concentration in Dars West-01. This difference is attributed to the higher water saturation in Jumman Shah-01, which reduces its effective hydrocarbon potential despite favorable porosity.

Discussion

Numerous studies conducted in Asia have applied seismic post-stack inversion methodologies to identify gas reserves. Band-limited impedance and post-stack model-based inversion have been used to evaluate the Krishna Godavari Basin, with results suggesting that this Cretaceous sedimentary stratum in this basin is analogous to those of the Southern Indus Basin in Pakistan (Gupta 2006; Ali et al., 2018). In the Krishna Godavari Basin of India, post-stack inversion has provided valuable insights for geological analyses, reservoir classification, and

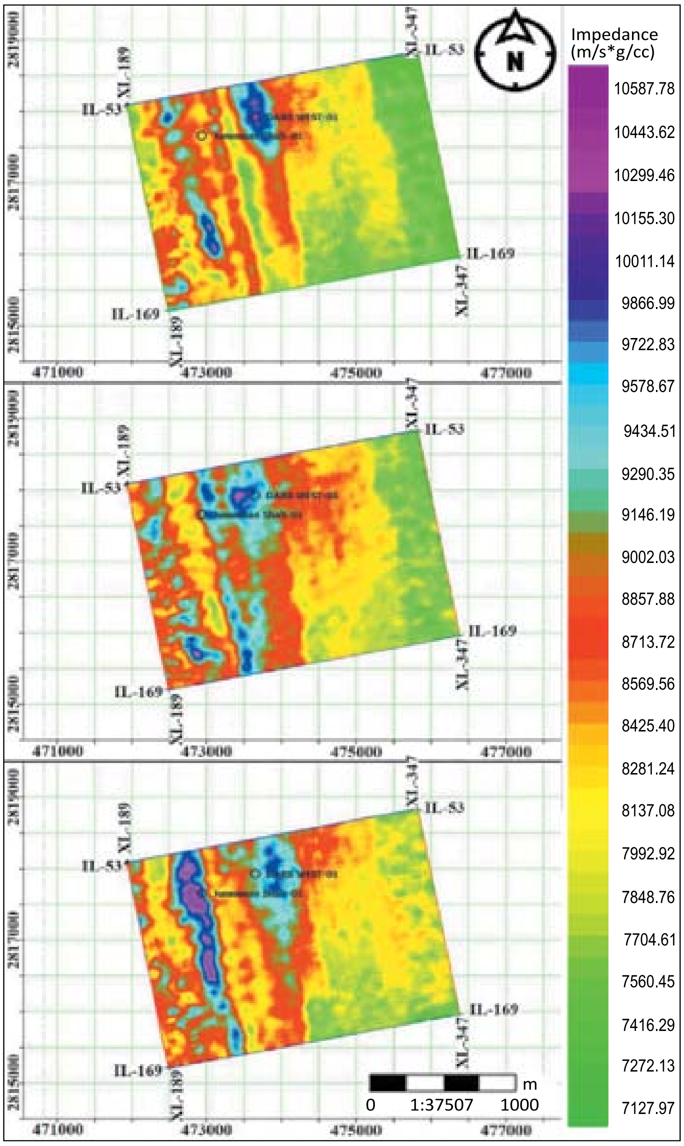

Figure 17. Acoustic impedance map of the B-Sand interval. Time slices are shown at (a) 1295 ms, (b) 1317 ms, and (c) 1338 ms, corresponding to depth intervals at Jumman Shah-01 of (a) 1535 m, (b) 1575 m, and (c) 1615 m

Rysunek 17. Mapy impedancji akustycznej poziomu piaszczystego B. Przedziały czasowe pokazano dla (a) 1295 ms, (b) 1317 ms i (c) 1338 ms, co odpowiada przedziałom głębokości w odwiercie Jumman Shah-01 wynoszącym około (a) 1535 m, (b) 1575 m i (c) 1615 m

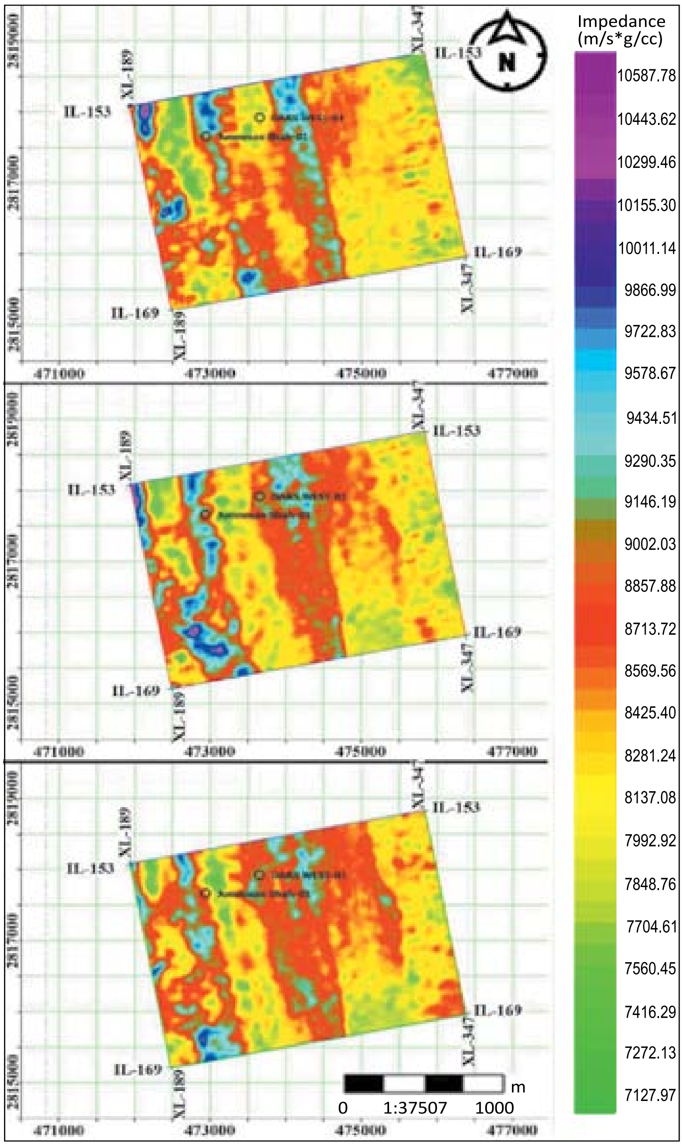

Figure 18. Acoustic impedance map of the B-Sand interval. Time slices are shown at (a) 1387 ms, (b) 1398 ms, and (c) 1409 ms, corresponding to depth intervals at DarsWest-01 of (a) 1860 m, (b) 1900 m, and (c) 1940 m

Rysunek 18. Mapy impedancji akustycznej poziomu piaszczystego B. Przedziały czasowe pokazano dla (a) 1387 ms, (b) 1398 ms i (c) 1409 ms, co odpowiada przedziałom głębokości w odwiercie DarsWest-01wynoszącym około (a) 1860 m, (b) 1900 m i (c) 1940 m

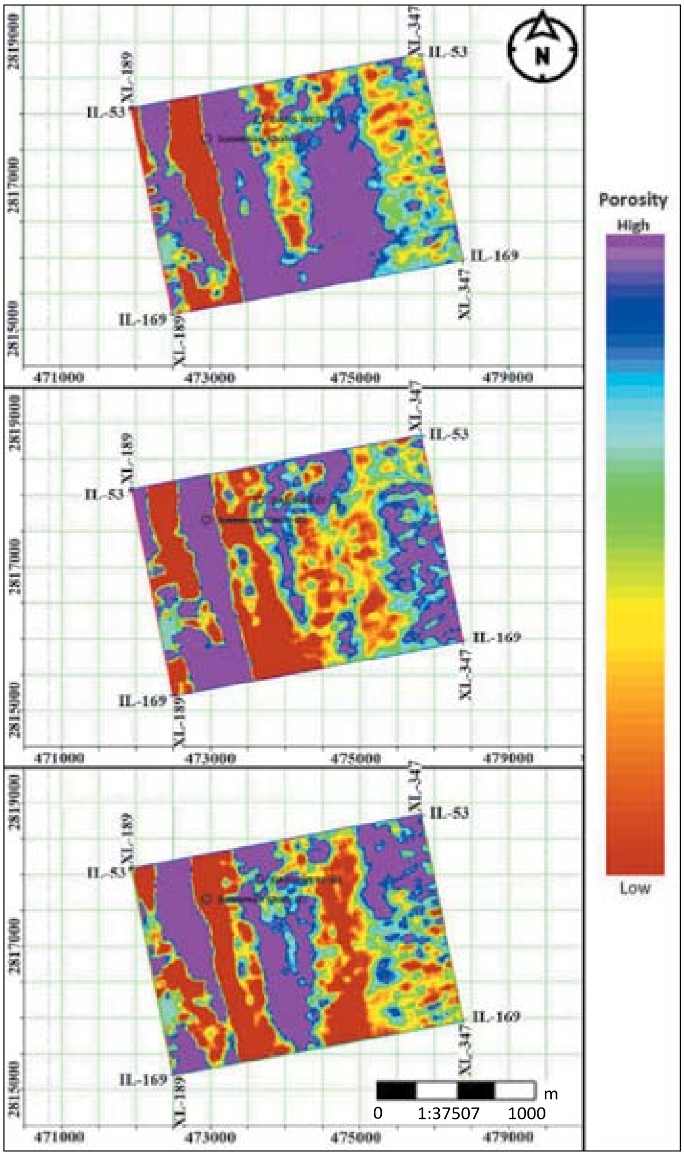

Figure 19. Porosity distribution within the B-Sand interval estimated from inverted impedance, overlain by the depth contour map. Time slices are shown at (a) 1295 ms, (b) 1317 ms, and (c) 1338 ms, corresponding to depth intervals at Jumman Shah-01 of (a) 1535 m, (b) 1575 m, and (c) 1615 m. At this location, porosity values derived from the model-based inversion and petrophysical analyses show good agreement

Rysunek 19. Rozkład porowatości w poziomie piaszczystym B oszacowany na podstawie odwróconej impedancji, nałożony na mapę konturów głębokości. Przedziały czasowe pokazano dla (a) 1295 ms, (b) 1317 ms i (c) 1338 ms, co odpowiada przedziałom głębokości w odwiercie Jumman Shah-01 wynoszącym około (a) 1535 m, (b) 1575 m i (c) 1615 m. W tej lokalizacji wartości porowatości uzyskane na podstawie inwersji opartej na modelu i analizy petrofizycznej wykazują dobrą zgodność

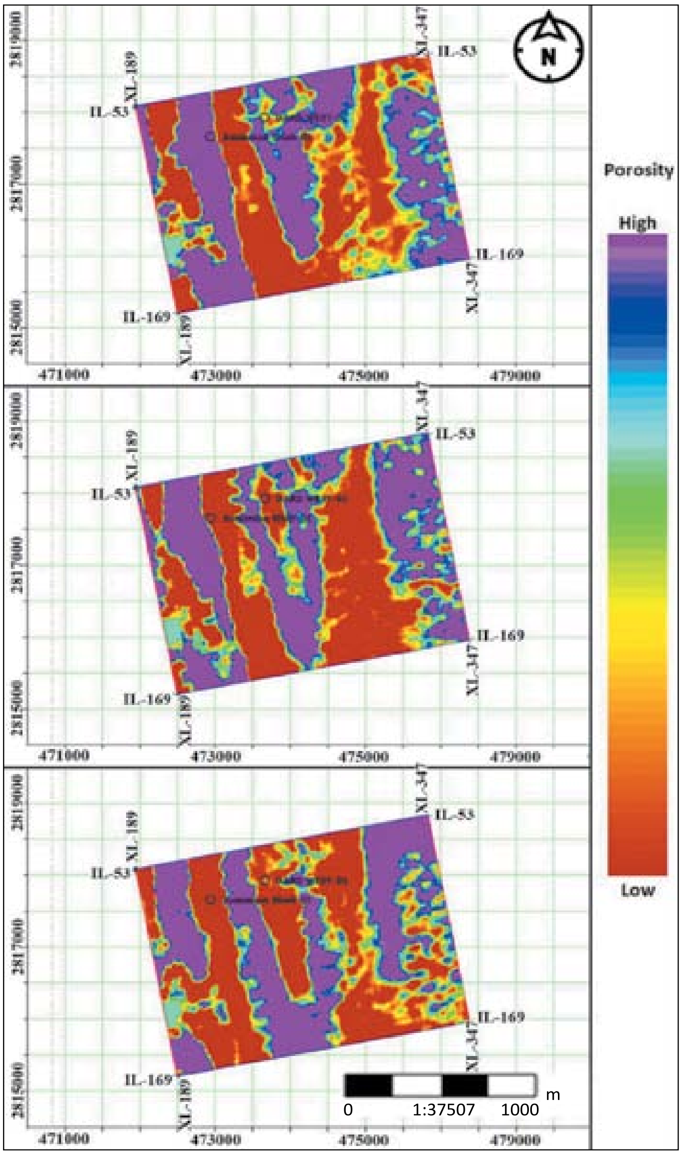

Figure 20. Porosity distribution within the B-Sand interval estimated from inverted impedance, overlain by the depth contour map. Time slices are shown at (a) 1387 ms, (b) 1398 ms, and (c) 1409 ms, corresponding to depth interval at DarsWest-01 of (a) 1860 m, (b) 1900 and (c) 1940 m. At this location, porosity values derived from the model-based inversion and petrophysical analyses show good agreement

Rysunek 20. Rozkład porowatości w poziomie piaszczystym B oszacowany na podstawie odwróconej impedancji, nałożony na mapę konturów głębokości. Przedziały czasowe pokazano dla (a) 1387 ms, (b) 1398 ms i (c) 1409 ms, co odpowiada przedziałom głębokości w odwiercie Dars West-01 wynoszącym około (a) 1860 m, (b) 1900 m i (c) 1940 m. W tej lokalizacji wartości porowatości uzyskane na podstawie inwersji modelowej i analizy petrofizycznej wykazują dobrą zgodność

delineation of prospective gas-bearing zones. According to these studies, inversion results reveal strong impedance contrasts that are interpreted as gas-saturated regions (Ali et al., 2018). In comparison with these findings, the band-limited and sparse-spike inversion techniques applied in the present study yield slightly lower-quality results than the model-based inversion. Similar analyses have been performed on the Ghar Formation in the Persian Gulf, Iran, using model-based inversion and cross-plots of inverted volumes to identify prolific hydrocarbon zones (Karabalaali et al., 2013). These studies also demonstrate that acoustic impedance contrasts within sand-shale successions are primarily associated with hydrocarbon saturation (Ali et al., 2018). The application of the three inversion techniques to seismic data volume in this study provides an acceptable estimation of acoustic impedance, which can be related to spatial sedimentological variability and used to classify hydrocarbon-bearing zones, particularly gas-saturated intervals. Using these three inversion approaches, gas-saturated regions within the B-Sand interval were successfully identified.

Porosity and permeability are critical parameters for determining reservoir characteristics; however, they are difficult to quantify accurately. These properties vary significantly with reservoir location and can be estimated properly only at well locations. To address this limitation, surface seismic data, petrophysical analysis, seismic inversion, and rock dynamics are integrated to achieve more reliable results (Leite and Vidal, 2011).

Accurate assessment of pore space within the reservoir is both essential and challenging. The presence of disseminated shale or multiple porosity types further complicates porosity estimation (Adekanle and Enikanselu, 2013). Several methods are available for porosity estimation, including wireline data interpretation and laboratory analysis of formation samples. Well data provide high vertical resolution and reliable porosity estimates at discrete locations; however, uneven well spacing makes it difficult to characterize reservoir properties, such as porosity distribution, between wells. Therefore, integrating the petrophysical results with seismic inversion outputs is essential to improve understanding of pore space distribution. Accordingly, acoustic impedance models derived from seismic inversion, together with reservoir parameters such as water saturation and porosity, play a key role in identifying reservoir zones between wells (Rijks and Jauffred, 1991).

Through geostatistical analysis, this study provides insights into reservoir classification and the spatial distribution of reservoir properties across the entire reservoir area. This approach represents a valuable methodology for characterizing sand-shale reservoirs in the Lower Indus Basin, Pakistan, and in other regions of Asia.

Conclusion

Effective reservoir characterization can be achieved through the integration of petrophysical analysis, geostatistical analysis, and inversion methods (inverted acoustic impedance). In this study, three inversion algorithms were applied and correlated to define reservoir characteristics in the NIM Block, Lower Indus Basin, Pakistan. The reservoir zones were specifically identified by all inversion algorithms used, and their spatial and lithological distributions were successfully delineated. Within the B-sand interval, inversion-based (estimated) porosity values range from 9% to 13% in Jumman Shah-01 and from 9% to 11% in Dars West-01. The average porosity of the B-sand intervals is approximately 16% in Jumman Shah and 11% in Dars West-01. Furthermore, the porosity estimates derived from post-stack inversion show good agreement with those obtained from petrophysical analysis for both wells. The reservoir characterization methodology applied in the Lower Indus Basin can be extended to other regions of Asia that exhibit similar geological conditions.

References

Abbasi S.A., Solangi S.H., Nazeer A., Asim S., Habib W., Solangi I.A., 2015. An Overview of Structural Style and Hydrocarbon Potential of Jabo Field, Southern Sindh Monocline, Southern Indus Basin, Pakistan. *Sindh University Research Journal-SURJ (Science Series)*, 47(2): 347–354.

Adekanle A., Enikanselu P.A., 2013. Porosity prediction from seismic inversion properties over 'XLD' Field, Niger Delta. *American Journal of Scientific and Industrial Research*, 4(1): 31–35. DOI: 10.5251/ajsir.2013.4.1.31.35.

Ahmad N., Fink P., Sturrock S., Mahmood T., Ibrahim M., 2004. Sequence stratigraphy as predictive tool in lower goru fairway, lower and middle Indus platform, Pakistan. *Pakistan Association of Petroleum Geoscientists*, 85–104.

Ahmed S., 2018. Study of Tectonic Evolution of Structures and Their Hydrocarbon Potential Using Seismic Data, Southern Sindh Monocline, Pakistan. Doctoral dissertation. *University of Sindh, Jamshoro*.

Ahmed S., Solangi S.H., Brohi I.A., Khokhar Q.D., Lashari R.A., 2014. Study of Stratigraphy and Structural Styles in the Subsurface of Southern Sindh Monocline, Pakistan: Using Seismic and Well Data. *Sindh University Research Journal-SURJ (Science Series)*, 46(4): 439–446.

Ahmed S., Solangi S.H., Jadoon M.S.K., Nazeer A., 2018. Tectonic evolution of structures in Southern Sindh Monocline, Indus Basin, Pakistan formed in multi-extensional tectonic episodes of Indian Plate. *Geodesy and Geodynamics*, 9(5): 358–366. DOI: 10.1016/j.geog.2018.03.004.

Ali A., Alves T.M., Saad F.A., Ullah M., Toqeer M., Hussain M., 2018. Resource potential of gas reservoirs in South Pakistan and adjacent Indian subcontinent revealed by post-stack inversion techniques. *Journal of Natural Gas Science and Engineering*, 49: 41–55. DOI: 10.1016/j.jngse.2017.10.010.

Ali A., Jakobsen M., 2014. Anisotropic permeability in fractured reservoirs from frequency-dependent seismic Amplitude Versus Angle and Azimuth data. *Geophysical Prospecting*, 62(2): 293–314. DOI: 10.1111/1365-2478.12084.

Anwer H.M., Alves T.M., Ali A., Zubair, 2017. Effects of sand-shale anisotropy on amplitude variation with angle (AVA) modelling: The Sawan gas field (Pakistan) as a key case-study for South Asia's sedimentary basins. *Journal of Asian Earth Sciences*, 147: 516–531. DOI: 10.1016/j.jseaes.2017.07.047.

Asquith G., Krygowski D., Henderson S., Hurley N., 2004. Basic well log analysis. *American Association of Petroleum Geologists*, 16. DOI: 10.1306/Mth16823.

Baig M.O., Harris N.B., Ahmed H., Baig M.O.A., 2016. Controls on reservoir diagenesis in the Lower Goru sandstone formation, Lower Indus Basin, Pakistan. *Journal of Petroleum Geology*, 39(1), 29–47. DOI: 10.1111/jpg.12626.

Banihasan N., Riahi M.A., Motavalli-Anbaran S.-H., 2006. Recursive and sparse spike inversion methods on reflection seismic data. *Institute of Geophysics, University of Tehran*.

Barclay F., Bruun A., Rasmussen K.B., Alfaro J.C., Cooke A., Cooke D., Salter D., Godfrey R., Lowden D., McHugo S., Ozdemir H., Pickering S., Pineda F.G., Herwanger J., Volterrani S., Murineddu A., Rasmussen A., Roberts R., 2008. Seismic inversion: Reading between the lines. *Oilfield Review*, 20(1): 42–63.

Chatterjee R., Singha D.K., Ojha M., Sen M.K., Sain K., 2016. Porosity estimation from pre-stack seismic data in gas-hydrate bearing sediments, Krishna-Godavari basin, India. *Journal of Natural Gas Science and Engineering*, 33(6): 562–572. DOI: 10.1016/j.jngse.2016.05.066.

Cooke D., Cant J., 2010. Model-based Seismic Inversion: Comparing deterministic and probabilistic approaches. *CSEG Recorder*, 35(4): 29–39.

Cooke D.A., Schneider W.A., 1983. Generalized linear inversion of reflection seismic data. *Geophysics*, 48(6): 665–676. DOI: 10.1190/1.1441497.

Downton J.E., 2005. Seismic parameter estimation from AVO inversion. Doctoral thesis. *University of Calgary, Department of Geology and Geophysics*, 3605–3605.

Doyen P.M., 1988. Porosity from seismic data: A geostatistical approach. *Geophysics*, 53(10): 1263–1275. DOI: 10.1190/1.1442404.

Droz L., Bellaiche G., 1991. Seismic facies and geologic evolution of the central portion of the Indus Fan. [In:] Weimer P., Link M.H. (eds). Seismic facies and sedimentary processes of submarine fans and turbidite systems. *Springer, New York*, 383–402.

Dubrule O., 2003. Geostatistics for seismic data integration in earth models. *Society of Exploration Geophysicists*, 6. DOI: 10.1190/1.9781560801962.

Gambús-Ordaz M., Torres-Verdín C., 2008. A study to assess the value of post-stack seismic amplitude data in forecasting fluid production from a Gulf-of-Mexico reservoir. *Journal of Petroleum Science and Engineering*, 62(1–2): 1–15. DOI: 10.1016/j.petrol.2008.06.001.

Gavotti P., Lawton D.C., Margrave G., Isaac J.H., 2013. Model-Based Inversion of Low-Frequency Seismic Data. *European Association of Geoscientists & Engineers 75th EAGE Conference & Exhibition incorporating SPE EUROPEC 2013*, 348. DOI: 10.3997/2214-4609.20130047.

Gavotti P.E., Lawton D.C., Margrave G.F., Isaac J.H., 2014. Post-stack inversion of the Hussar low frequency seismic data. *CREWES Research Report*, 24: 1–22.

Gupta S.K., 2006. Basin architecture and petroleum system of Krishna Godavari Basin, east coast of India. *The Leading Edge*, 25(7): 830–837. DOI: 10.1190/1.2221360.

Hampson D.P., Schuelke J.S., Quirein J.A., 2001. Use of multiattribute transforms to predict log properties from seismic data. *Geophysics*, 66(1): 220–236. DOI: 10.1190/1.1444899.

Huuse M., Feary D.A., 2005. Seismic inversion for acoustic impedance and porosity of Cenozoic cool-water carbonates on the upper continental slope of the Great Australian Bight. *Marine Geology*, 215(3–4): 123–134. DOI: 10.1016/j.margeo.2004.12.005.

Ibrahim M., 2007. Seismic Inversion Data, a Tool for Reservoir Characterization/ Modeling Sawan Gas Field – a Case Study. *Pakistan Association of Petroleum Geoscientists, Annual Technical Conference*.

Jain C., 2013. Effect of seismic wavelet phase on post stack inversion. [In:] *10th Biennial International Conference & Exposition, Kochi*, 1–410.

Jamil A., Waheed,A., Sheikh R.A., 2012. Pakistan's major petroleum plays-An Overview of Dwindling Reserves. *AAPG Search and Discovery Article*, 10399: 1–2.

Karbalaali H., Shadizadeh S.R., Riahi M.A., 2013. Delineating Hydrocarbon Bearing Zones Using Elastic Impedance Inversion: A Persian Gulf Example. *Iranian Journal of Oil & Gas Science and Technology*, 2(2): 8–19. DOI: 10.22050/ijogst.2013.3534.

Khalid P., Ehsan M.I., Akram S., Din Z.U., Ghazi S., 2018. Integrated Reservoir Characterization and Petrophysical Analysis of Cretaceous Sands in Lower Indus Basin, Pakistan. *Journal of the Geological Society of India*, 92(4): 465–470.

Krebs J.R., Anderson J.E., Hinkley D., Neelamani R., Lee S., Baumstein A., Lacasse M.D., 2009. Fast full-wavefield seismic inversion using encoded sources. *Geophysics*, 74(6): WCC177–WCC188.

Kumar R., Das B., Chatterjee R., Sain K., 2016. A methodology of porosity estimation from inversion of post-stack seismic data. *Journal of Natural Gas Science and Engineering*, 28: 356–364. DOI: 10.1016/j.jngse.2015.12.028.

Leite E.P., Vidal A.C., 2011. 3D porosity prediction from seismic inversion and neural networks. *Computers & Geosciences*, 37(8): 1174–1180. DOI: 10.1016/j.cageo.2010.08.001.

Li Q., 2001. LP sparse spike inversion. Strata Technique Document. *Hampson-Russell Software Services Ltd*.

Lindseth R.O., 1979. Synthetic sonic logs; A process for stratigraphic interpretation. *Geophysics*, 44(1): 3–26. DOI: 10.1190/1.1440922.

Maurya S.P., Singh K.H., 2015. LP and ML sparse spike inversion for reservoir characterization-a case study from Blackfoot area, Alberta, Canada. *77th EAGE Conference and Exhibition 2015. European Association of Geoscientists & Engineers*, 2015(1): 1–5. DOI: 10.3997/2214-4609.201412822.

Maurya S.P., Singh N.P., 2017. Seismic colored inversion: A fast way to estimate rock properties from the seismic data. *Carbonate reservoir workshop*, November 30.

Maurya S.P., Singh N.P., 2018. Comparing pre-and post-stack seismic inversion methods-a case study from Scotian Shelf, Canada. *Journal of Indian Geophysical Union*, 22(6): 585–597.

Maurya S.S., Singh N.P., Singh K.H., 2020. Seismic Inversion Methods: A Practical Approach. *Springer Nature*.

Oldenburg D.W., Scheuer T., Levy S. 1983. Recovery of the acoustic impedance from reflection seismograms. *Geophysics*, 48(10): 1318–1337. DOI: 10.1190/1.1441413.

Ontiveros T., Herrera V., Meza R., 2014. Seismic Inversion Applied to Geological and Operational Monitoring of Drilling Horizontal Wells in the Carabobo Area of the Faja Petrolífera del Orinoco. *Heavy Oil Latin America Conference and Exhibition*.

Rijks E.J.H., Jauffred J.C.E.M., 1991. Attribute extraction: An important application in any detailed 3-D interpretation study. *The Leading Edge*, 10(9): 11–19. DOI: 10.1190/1.1436837.

Russell B., 1992. Seismic Inversion: Part 7. Geophysical Methods. *American Association of Petroleum Geologists*, 395–397.

Sheikh N., Giao P.H., 2017. Evaluation of shale gas potential in the lower cretaceous Sembar formation, the southern Indus basin, Pakistan. *Journal of Natural Gas Science and Engineering*, 44: 162–176. DOI: 10.1016/j.jngse.2017.04.014.

Torres-Verdín C., Sen M.K., 2004. Integrated approach for the petrophysical interpretation of post-and pre-stack 3-D seismic data, well-log data, core data, geological data, geological information and reservoir production data via Bayesian stochastic inversion. *University of Texas Center for Petroleum and Geosystems Engineering & Institute for Geophysics*.

Veeken P.C.H., Da Silva A.M., 2004. Seismic inversion methods and some of their constraints. *First Break*, 22: 47–70. DOI: 10.3997/1365-2397.2004011.

Wandrey C.J., Law B.E., Shah H.A., 2004. Sembar Goru/Ghazij composite total petroleum system, Indus and Sulaiman-Kirthar geologic provinces, Pakistan and India. *U.S. Geological Survey Bulletin 2208-C*.

Wang Y., 2016. Seismic inversion: theory and applications. *John Wiley & Sons*.

Yilmaz Ö., 2001. Seismic data analysis: Processing, inversion, and interpretation of seismic data. *Society of Exploration Geophysicists*.

Zehra S., Afsar S., 2016. Flood hazard mapping of lower indus basin using multi-criteria analysis. *Journal of Geoscience and Environment Protection*, 4(04): 54–62. DOI: 10.4236/gep.2016.44008.

Muyyassar HUSSAIN, Ph.D.
Principal Geoscientist at LMKR, Pakistan;
Geophysical & Data Management Technology Center
9th Floor Ufone Tower, Blue Area, Islamabad, Pakistan
E-mail: *muyyassarhussain@lmkr.com*

Furqan Mahmud BUTT, Ph.D.
Research Associate at COMSATS University Islamabad
Park Road, Tarlai Kalan, Islamabad 45550, Pakistan
E-mail: *furqan.mahmud@comsats.edu.pk*

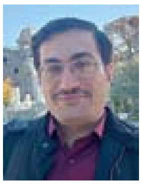

Sarfraz KHAN, Ph.D.
Assistant Professor at the National Centre of Excellence in Geology, University of Peshawar
Rahat Abad, Peshawar, 25130, KP, Pakistan
E-mail: *sarfraz_nceg@uop.edu.pk*

Umair Bin NISAR, Ph.D.
Assistant Professor at COMSATS University Islamabad
Park Road, Tarlai Kalan, Islamabad 45550, Pakistan
E-mail: *umair.nisar@comsats.edu.pk*

Shuja ULLAH, Ph.D.
Research Assistant at the National Centre of Excellence in Geology, University of Peshawar
Rahat Abad, Peshawar, 25130, KP, Pakistan
Ministry of Energy, Petroleum Division, Geological Survey of Pakistan, Islamabad
Sector B-1, Phase 5, Peshawar, KP, Pakistan
E-mail: *shuja_nceg@uop.edu.pk*